# New particle formation in the Svalbard region 2006 - 2015

Jost Heintzenberg[1], Peter Tunved[2], Martí Galí[3], and Caroline Leck[4]

1: Leibniz Institute for Tropospheric Research (TROPOS), Permoserstr. 15, 04318 Leipzig, Germany
2: Department of Environmental Science and Analytical Chemistry (ACES), Stockholm University, 10691 Stockholm, Sweden
3: Takuvik Joint International Laboratory & Québec-Océan, Université Laval, G1V 0A6 Québec, Canada
4: Department of Meteorology, Stockholm University (MISU), 10691 Stockholm, Sweden

Abstract

Events of new particle formation, (NPF), were analyzed in a ten-year data set of hourly particle size distributions recorded on Mt. Zeppelin, Spitsbergen, Svalbard. Three different types of NPF-events were identified through objective search algorithms. The first and simplest algorithm utilizes short-term increases in particle concentrations below 25 nm, (PCT-events). The second one builds on the growth of the sub-50 nm diameter-median, (DGR-events), and is most closely related to the classical "banana-type" of events. The third and most complex, so-called multiple-size approach to identifying NPF-events builds on a hypothesis suggesting the concurrent production of polymer gel particles at several sizes below about 60 nm, (MEV-events).

As a first and general conclusion we can state that NPF-events are a summer phenomenon and not related to Arctic haze, which is a late winter-to-early spring feature. The occurrence of NPF-events appears to be somewhat sensitive to the available data on precipitation. The seasonal distribution of solar flux suggests some photochemical control that may affect marine biological processes generating particle precursors and/or atmospheric photochemical processes that generate condensable vapors from precursor gases. Notable, the seasonal distribution of the biogenic methanesulfonate, (MSA), follows that of the solar flux although it peaks before the maxima in NPF-occurrence.

A host of ancillary data and findings point to varying and rather complex marine biological source processes. The potential source regions for all types of new particle formation appear to be restricted to the marginal ice and open water areas between Northeastern Greenland and Eastern Svalbard. Depending on conditions yet to be clarified new particle formation may become visible as short bursts of particles around 20 nm, (PCT-events), longer events involving condensation growth, (DGR-events), or extended events with elevated concentrations of particles at several sizes below 100 nm, (MEV-events). The seasonal

distribution of NPF-events peaks later than that of MSA and, DGR and in particular of MEV-events reach into late summer and early fall with much open, warm, and biologically active waters around Svalbard. Consequently, a simple model to describe the seasonal distribution of the total number of NPF-events can be based on solar flux, and sea surface temperature, representing environmental conditions for marine biological activity, and condensation sink, controlling the balance between new particle nucleation and their condensational growth. Based on the sparse knowledge about the seasonal cycle of gel-forming marine microorganisms and their controlling factors we hypothesize that the seasonal distribution of DGR and more so MEV-events reflect the seasonal cycle of the gel-forming phytoplankton.

## 1. Introduction

In the late 1970ies and early 1980ies the interest in the Arctic atmospheric aerosol widened from the well-identified winter phenomenon of Arctic haze (Rahn and Shaw, 1977; Heintzenberg and Leck, 1994) to summer conditions in this northernmost remote region. In the pristine Arctic summer air the so-called background aerosol (Junge, 1963) was expected to be most clearly visible, far away from the northern hemispheric anthropogenic emission centers at lower latitudes. Episodic and localized occurrences of high concentrations of ultrafine particles, (here defined as particles with diameters < 100 nm), in the summer Arctic were explained by rare import of polluted air from lower latitudes (Flyger and Heidam, 1978; Heintzenberg and Larssen, 1983) or hypothetical anthropogenic sources in the Arctic (Jaenicke and Schütz, 1982).

With the advent of sensitive condensation nuclei counters (Agarwal and Sem, 1980) and differential mobility analyzers (Knutson and Whitby, 1975b, a) more details became visible in the Arctic sub-micrometer aerosol. High numbers of ultrafine particles were observed in connection with fog passages (Lannefors et al., 1983) and chemical aerosol information indicated a regional – possibly biogenic – particle sources in the summer Arctic (Heintzenberg, 1989). The high molar ratios of methane sulfonate, (MSA), to non-sea salt sulfate, ($nssSO_4^{2-}$), of 0.28 in the Arctic summer aerosol found by Heintzenberg and Leck (1994) substantiated the biogenic source of the particles.

The establishment of long-term Arctic aerosol monitoring at the fringes of the pack ice in Alaska (e.g., Polissar et al., 1999), Canada (e.g., Norman et al., 1999; Willis et al., 2016), and on Spitsbergen (e.g., Tunved et al., 2013) revealed more details of potential sources of the summer aerosol, in particular their connection to the marine biosphere in the Arctic. The unique series of systematic aerosol studies in the central Arctic north of 80°N onboard the Swedish icebreaker *Oden* in 1996 led to the formulation of a new hypothesis concerning a

specific process of marine biogenic particle formation (Leck and Bigg, 1999). The marine biogenic particles involved behaved as polymer gels and originated in the surface microlayer (SML) of the ocean, (Orellana et al., 2011b), from the activity of sea-ice algae, phytoplankton and, perhaps, bacteria. The new particle events were reported to occur as simultaneous enhancement of particle number concentrations in the whole size-range below 50 nm, and not with the prototypical "banana growth" (Kulmala et al., 2004). Two more *Oden* cruises in 2001 and 2008 yielded results that were partly contradicting (Held et al., 2011b; Held et al., 2011a), partly supporting the SML hypothesis (Leck et al., 2013; Karl et al., 2013; Orellana et al., 2011b; Leck and Bigg, 2010). The synopsis of the results of four *Oden* cruises of Heintzenberg et al. (2015) identified geographic regions of new particle formation (NPF) in the inner Arctic while stressing the importance of recent open water and related biological activity in the sea in transects by air masses with new particle formation over the central Arctic.

Two years of aerosol size distributions from Mt. Zeppelin, Spitsbergen and Alert, both located at the fringes of the central pack ice, were analyzed by Croft et al. (2016a) with a global aerosol geophysics model. They discuss classical new-particle nucleation, coagulation scavenging in clouds, scavenging by precipitation, and transport in order to explain the annual cycle of the Arctic aerosol. Croft et al. (2016a) find two seasonal maxima in their modeled particle nucleation rates, one in March, and one in July. In spring, their simulated NPF occurs mainly in the free troposphere, whereas in summer, it occurs also in the planetary boundary layer. More recently, Croft et al. (2016b) state that ammonia from seabird-colony guano is a key factor contributing to bursts of newly formed particles, which are observed every summer in the near-surface atmosphere, at least at Alert, Nunavut, Canada. Earlier, the results of studies with another global aerosol model by Browse et al. (2014) suggested that the potential increase in NPF in the Arctic with potential increases in cloud condensation nuclei is

compensated by wet scavenging. They also state that scavenging by pre-existing large particles suppresses NPF-events.

Based on three years of data from the two Arctic sites Thule and Ny-Ålesund (gruvebadet) Becagli et al. (2016) examined the sources and environmental factors controlling the biological aerosol component MSA. Their analysis included satellite-derived Chlorophyll-*a* (an indicator of phytoplankton biomass), oceanic phytoplankton primary productivity, (PPP), and sea ice. Whereas they found good correlations between MSA, PPP and sea ice, (the latter two being closely related), their data did not allow any statements on NPF processes.

To date the longest record of sub-micrometer number-size distributions of the Arctic aerosol down to 5 nm particle diameter and below has been accumulated on Mt. Zeppelin, Spitsbergen (Tunved et al., 2013; Heintzenberg and Leck, 1994). For the ten years from 2006 through 2015 a total of 63936 quality-controlled hours of aerosol data are available, i.e. during 73% of all hours of the ten years. In the present study we exploit this formidable data set in a search for processes forming new particles. An important first step in this work was formulating completely objective criteria for the identification of events. In the relatively clean Arctic environment we do not expect the classical nucleation and growth events as frequently observed over the continents, (cf. Kulmala et al., 2004), to dominate. Thus, we refrained from applying the objective search algorithm formulated by Heintzenberg et al., (2007) for this "Banana-type" of events. Instead we formulated new objective search algorithms allowing several potential types of new particle formation events or formation processes. With a host of complementary atmospheric and surface physical, chemical, and biological information a large number of NPF-events identified with these algorithms will be analyzed in the following chapters.

## 2. Database

The Mt. Zeppelin observatory

Situated at the top of Mt Zeppelin, Svalbard (78° 56'N, 11° 53'E), the Zeppelin observatory offers a unique possibility to study the characteristic features of Arctic atmospheric constituents such as trace gases and aerosol particles. At a height of 474 m a.s.l. the station is located near the top of the local planetary boundary layer and represents remote Arctic conditions. The closest source of pollution, the small community of Ny-Ålesund, is located ~2 km north of the station (http://www.esrl.noaa.gov/psd/iasoa/sites/default/files/stations/nyalesund/nyalesund_site.jpg). However, the elevation difference and typical wind patterns largely prevent pollution from nearby sources to reach the Zeppelin Observatory. The dominating wind pattern is east-southeast katabatic flow from Kongsvegen glacier or from northwesterly directions as channeled by the Kongsfjord (Beine et al., 2001; Heintzenberg et al., 1983). The station itself was initially established in 1991, and is owned by the Norwegian Polar Research Institute (NP). The Norwegian Institute for Air Research (NILU) is responsible for the coordination of the scientific program.

### 2.1 Physical aerosol data

After a period of continuous aerosol measurements by the Department of Meteorology, Stockholm University in the early 1990ties, (Heintzenberg and Leck, 1994), the Department of Analytical Chemistry and Environmental Science, Stockholm University, initialized observations of the aerosol number size distribution in mid-2000. Originally, the system

consisted of a single differential mobility analyzer system, (DMPS), consisting of a medium-size Hauke-type differential mobility analyzer, (DMA), together with a TSI 3760 condensation particle counter, covering diameters between 20 and ~500nm. From 2006 on the particle size range was widened covering particle sizes between 10 and 790 nm. In 2005, the rain-cover over the inlet was replaced. Initially, the instrument inlet was of a PM10 type, removing particles or hydrometeors with diameters >10 μm from the sampled air stream. During a substantial renewal of the Stockholm University equipment in 2010-2011, both inlet and DMPS system were replaced.

Since then, the DMPS-system utilizes a custom-built twin DMA-setup comprising one Vienna-type medium DMA coupled to a TSI CPC 3010 covering sizes between 25-800 nm and a Vienna-type long DMA coupled with at TSI CPC 3772 covering sizes between 5-60 nm. The size distributions from the two systems are harmonized on a common size grid and then merged. Both systems use a closed-loop flow setup. The current inlet hat is of whole air type, complying with EUSAAR[1] standard for high altitude or Arctic sampling conditions. In the current setup, the inlet is operated with a flow of ca. 100 liters per minute, (lpm). Laminar flow conditions apply throughout the sampling lines. Outside of the station, the inlet temperature is kept above 0°C using active heating. Inside the station the temperature increases gradually to room temperature (maximum temperature reaches ca. 25 °C, but remains typically around 20°C). Relative humidity, (RH) and temperature are internally monitored and measurements are maintained at dry conditions with RH < 30%. The system is regularly checked with latex spheres and flow controls. The recorded data are manually screened and crosschecked with other available observation as in Tunved et al. (2013). If inconsistencies were found between the different datasets, further investigation was

[1] EUSAAR (European Supersites for Atmospheric Aerosol Research) is an EU-funded I3 (Integrated Infrastructures Initiatives) project carried out in the FP6 framework of the specific research and technological development gram "Structuring the European Research Area - Support for Research Infrastructures", (http://www.eusaar.net/).

performed to exclude data that were identified as affected by instrumental errors. Using the instrumental logbook, periods of local activity potentially influencing the sampling were also excluded from the dataset. During the years 2006 – 2010 no particles below ten nanometers in diameter were recorded. From 2011 on four more diameter bins down to 5 nm were included and a different diameter array was utilized. To allow for a synopsis of all years all size distributions were interpolated on the pre-2011 diameter array and all integrals of the size distribution over particle diameter were taken over the joint diameter range 10 to 631 nm. For the pre-2011 years the data at the four size channels below 10 nm were flagged as missing. However, whenever results cover the complete time series the resulting number concentrations in the four first channels covering the years 2011 – 2015 are carried along.

For the identification of NPF in terms of particle growth the parameter D50 in nanometer was calculated as the number median diameter of particles smaller than 50 nm but larger than 10 nm, i.e. 50% of all particles below that size are smaller than D50. Besides this parameter Table 1 lists nine integral particle parameters, which are utilized in the NPF-search approaches or in the interpretation of results. These aerosol parameters quantify total particle number, (NTO), and particle numbers in sub-ranges of the number size distribution such as N25, quantifying the total number of particles between ten and 25 nm.

Following the concept developed by Pirjola et al., (1999), and Kulmala et al., (2001) we calculated the condensation sink, (CS, $s^{-1}$), as a parameter with which the probability of new particle formation from the gas phase and the necessary amount of condensable vapor can be estimated. We utilized number size distributions, pressure and temperature taken from our database for this calculation.

## 2.2 Chemical aerosol data

For the interpretation of NPF-events we employed chemical information derived from the analyses of high volume particle samples taken by the Norwegian Institute for Air research, (NILU). A high volume sampler (PM10) was used to collect samples for a quantitative determination of sodium, ($Na^+$), sulfate, ($SO_4^{2-}$) and MSA ($CH_3SOO^-$). The sampler collected material for analysis in one to three days. Blank samples were obtained by mounting the glass fiber filters at the sampling site with the same sampling period but without air passing through. $Na^+$ and $SO_4^2$ were analyzed by NILU and have been downloaded for the present study from the EBAS database (http://ebas.nilu.no), which list details about the sampling technique and the sampling protocol. Nss $SO_4^{2-}$ was determined from total sulfate correcting for sea salt sulfate as $0.25 x Na^+$, (Keene et al., 1986).

MSA was analyzed at the laboratory of the Department of Meteorology, Stockholm University. To allow for subsequent chemical determinations the ambient samples and blanks were carefully handled in a glove box (free from particles, sulfur dioxide and ammonia). At the time of the chemical analyses, still in the glove box, the substrates were extracted (in centrifuge tubes) with 60 $cm^3$ deionized water (Millipore Alpha-Q, conductivity 18 MΩcm). The extracts were thereafter analyzed for weak anions by chemically suppressed ion chromatography (IC, Dionex ICS-2000) using Dionex AG11/AS11 columns. In order to trap carbonates and other ionic contaminants a Dionex ATC-1 column was used before the injection valve. The injection volume was 50 $\mu dm^3$. Quality checks of the IC-analyses were performed with both internal and external reference samples (Das et al., 2011). The analytical detection limits obtained for the various ions, defined as twice the level of peak-to-peak instrument noise, was 0.0001 $\mu eq\ dm^{-3}$ for MSA. The overall analytical accuracy was better than 1.5%.

## 2.3 Back-trajectories and meteorological data

For every hour during the ten years 2006 through 2015 three-dimensional back trajectories have been calculated arriving at 474 m at Mt. Zeppelin. The trajectories have been calculated backward for up to ten days using the HYSPLIT4 model (Draxler and Rolph, 2003) with meteorological data from the Global Data Assimilation System with one-degree resolution (GDAS1). Trajectories extending backwards for ten days are inaccurate at origin due to the trajectory uncertainty of 25-30% of its length, (Stohl, 1998). More information about the GDAS dataset can be found at Air Resources Laboratory (ARL), NOAA (http://ready.arl.noaa.gov), from which the meteorological data were downloaded.

During the analyzed time period meteorological records at the Mt. Zeppelin station are rather limited in quality and were frequently interrupted. There are no precipitation measurements and wind measurements are strongly influenced by the station building and by the local topography. In order to have an internally consistent, and unbroken meteorological record we utilized hourly meteorological parameters at trajectory arrival times as calculated by the HYSPLIT4 model. We emphasize that their accuracy depends on the quality of the meteorological model inside HYSPLIT4 and the accuracy and representativeness of the meteorological fields utilized by the model. Of the local meteorological record air temperature was considered the most reliable and thus explored in a comparison of trajectory calculated and modeled meteorological data. When comparing the 42600 contiguous hourly records from 2008-01-01 until 2012-11-10 the average ratio of measured and calculated temperatures is 0.98, with a coefficient of determination of 0.96. The utilized model parameters are listed in Table 1.

As an additional parameter we evaluated the vertical air movement of the trajectories during the last hour before arrival by subtracting the trajectory height one hour before arrival

257 at the arrival height of 474 meter. The resulting vertical displacement parameter, DZ, is given
258 in meters per hour. Positive values of DZ indicate a lifting of the air.
259 The most important missing meteorological information concerns the local cloud cover.
260 No direct recording was available of times during which the station was in clouds. The
261 closest available cloud instrument is a ceilometer operated by the Alfred Wegener Institute
262 (AWI) at their Koldewey Station in Ny-Ålesund, i.e. in the valley below Mt. Zeppelin, some
263 2.8 km of horizontal distance from the position of the mountain station. From the one-minute
264 records of the ceilometer we derived hourly values of the 25% percentile of cloud base, which
265 was used as an indicator for the Zeppelin station being in cloud. This ceilometer parameter is
266 listed as C25 in Table 1.
267 Precipitating clouds scavenge the planetary boundary layer and thus reduce the available
268 particle surface as condensation sink of particle precursors. As a consequence nucleation
269 from the gas phase may be facilitated (Tunved et al., 2013). As in Tunved et al. (2013) we
270 utilized the HYSPLIT-modeled precipitation along the back trajectories. Sums of
271 precipitation, (SP, see Table 1), were calculated along each back trajectory and will be
272 referred to as SP1 (during the last day), SP2 (during the last but one day), and SP5 (during
273 days three to five) before arrival at Mt. Zeppelin.
274
275
276 **2.4 Marine biological data**
277
278 The biologically active marginal ice zone is a major natural source of sulfur in the Arctic
279 summer atmosphere, (Leck and Persson, 1996b, a), and Wiedensohler et al. (1996), indicated
280 a potentially important role of dimethyl sulfide (DMS) in regional new particle formation.
281 DMS emissions from the sea have long been proposed to control new particle formation in the
282 marine boundary layer, (Charlson et al., 1987), which builds on $DMS_{aq}$ being transported via

turbulence and diffusion to the sea-air interface, represented by the transfer velocity, which in turn depends on sea-surface temperature, salinity, and wind speed, (Liss and Merlivat, 1986). Once in the atmosphere $DMS_g$ is photochemical oxidized via intermediates such as sulfuric acid and methane sulfonic acid, (Ayers et al., 1996), which eventually leads to the formation of aerosol $nssSO_4^{2-}$ and MSA. The products of the photochemical oxidation of DMS the ratio MSA/ $nssSO_4^{2-}$ show a temperature dependence (Bates et al., 1990), favoring MSA in the cold Arctic environment (Karl et al., 2007).

Dimethyl sulfide in the ocean ($DMS_{aq}$) is produced through the degradation of its algal precursor dimethylsulfoniopropionate (DMSP) by microbial food webs, (Simó, 2001). At high latitudes, total DMSP (DMSPt) and therefore $DMS_{aq}$, essentially follows the seasonal cycle of phytoplankton biomass, (Lana et al., 2012). DMSPt is defined as the sum of $DMSP_{dissolved}$ and $DMSP_{particulate}$ concentration. Yet, the amount of DMSPt per unit phytoplankton biomass may vary depending on species composition and physiological state, (Keller et al., 1989).

The dissolved organic carbon (DOC) concentrations in surface waters of the high Arctic Ocean are up to ten times higher than in any other ocean basin and closer in range to DOC levels reported for sea ice (Gao et al., 2012). A large fraction of DOC spontaneously assembles into polymer gels: polysaccharide forming hydrated calcium bonded three-dimensional networks to which other organic compounds, such as proteins and lipids, are readily bound. The assembly and dispersion of the polysaccharide molecules can be affected by environmental parameters, such as UV-B radiation (280-320nm) dispersing or inhibiting gel formation, and/or pH and temperature inducing gel volume phase changes (swelling and shrinkage). In the study of Orellana et al., (2011b), the swelling and shrinking of the polysaccharide networks or polymer gels were also causally related by additions of nano to micromolar levels of DMS and DMSP. High DMSP concentrations have also been measured

in the mucilage surrounding prymnesiophyte *Phaeocystis pouchetii* colonies in Arctic waters, representing up to 25% of the total water column DMSP pool, (Matrai and Vernet, 1997). The findings made by Orellana et al., (2011b) were in agreement with previous findings by Orellana et al., (2011a) that high concentrations of DMSP and DMS are stored in the acidic secretory vesicles of the *Phaeocystis* algae where DMSP is trapped within the condensed polyanionic gel matrix until the secretory vesicles are triggered by environmental factors such as temperature to release gels that undergo volume phase transition and expand at the higher pH of seawater. Exocytosis of polymer gels accompanied by elevated DMS and DMSP concentrations suggests the transport of these chemical compounds by the gel matrix. Schoemann et al., (2005) report that *Phaeocystis antarctica* is particularly well adapted to low temperatures, being more competitive than *P. pouchetii for temperatures between* -2 and +2 °C. *Phaeocystis pouchetii*, however, appears to be better adapted to temperatures closer to 5 °C. In the Arctic a higher occurrence of the *Phaeocystis pouchetii* would be expected in the northward advection of warm Atlantic water masses around Svalbard.

Here we estimated DMSPt at the sea surface using the algorithm described by Galí et al. (2015). The DMSPt algorithm exploits the distinct relationship between DMSPt and Chlorophyll-*a* depending on the light exposure regime of the phytoplankton community. The light exposure regime is defined by the ratio between euphotic layer depth and mixed layer depth ($Z_{eu}$/MLD). Additional predictor variables used are sea surface temperature (SST) and particulate inorganic carbon (PIC), which is used in the algorithm as a proxy for coccolitophores such as *Emiliania huxleyi*. During late bloom stages, the calcite plates that cover coccolitophore cells (called coccoliths) detach and cause an increase in seawater backscatter that invalidates satellite retrievals of Chlorophyll-*a*. Therefore, inclusion of PIC in the algorithm as a proxy for DMSPt increases data coverage. Although the algorithm was developed for the global ocean, validation results with in situ data indicate that it performs as well or slightly better in Arctic and sub-Arctic waters.

334 The use of remotely sensed DMSPt as a proxy for marine DMSaq emission is a significant
335 improvement with respect to prior studies that used Chlorophyll-*a* (Becagli et al., 2016;
336 Zhang et al., 2015). Yet, it is not ideal because (i) the ratios $DMS_{aq}$/DMSPt in surface
337 seawater are variable, and tend to be higher in high solar irradiance and nutrient-poor
338 conditions typical of summer, (Galí and Simó, 2015), and (ii) even if DMSPt is a better proxy
339 for $DMS_{aq}$, the influence of meteorological and sea surface conditions (mainly wind speed
340 and SST) on the sea-air flux of $DMS_{aq}$ is not taken into account. Development is underway of
341 an algorithm for the retrieval of $DMS_g$ concentrations in air and DMS fluxes.
342 The DMSPt algorithm was run for the 2006-2015 period using daily composites of the
343 Moderate Resolution Imaging Spectroradiometer on the Aqua satellite (MODIS-Aqua) at 4.64
344 km resolution (L3BIN, reprocessing R2014.0) downloaded from NASA's Ocean Color
345 website (http://oceancolor.gsfc.nasa.gov). The MODIS variables used include Chlorophyll-*a*
346 concentration derived with the GSM algorithm, (Maritorena et al., 2002), PIC, nighttime SST
347 and $Z_{eu}$. MODIS nighttime SST was complemented with SST from the Advanced Very High
348 Resolution Radiometer (AVHRR, https://podaac.jpl.nasa.gov/AVHRR-Pathfinder) to increase
349 data availability. MLD was obtained from the MIMOC climatology, (Schmidtko et al.,
350 2013), which was linearly interpolated from its original 0.5°x0.5° grid at monthly resolution
351 to the MODIS grid at daily resolution.
352 Satellite remote sensing of biological activity in surface waters requires ice-free and at
353 least part of the time cloud-free. The passive sensing methods of MODIS additionally require
354 a minimum of solar illumination of the scenes (i.e., solar zenith angle < 70°; (IOCCG, 2015)).
355 Consequently, the length of the satellite-observable period used to compute DMSPt means
356 shortens from all-year-round at latitudes <45° to approximately six months (the spring-
357 summer semester) at 80°N. In addition, the annual DMSPt map in Fig. 3 excludes all land and
358 ice covered regions. In order to increase data coverage, daily DMSPt composites were binned
359 to five-day periods and a 46.4 km equal-area sinusoidal grid, (10x10 bins of the original pixel

size). The average distance between a trajectory point and the closest center of a MODIS pixel is 18 km.

Following the same approach as with the ice data average DMSPt from ocean color data, (OC), along each back trajectory were calculated and will be referred to as OC1 (the last day), OC2 (the last but one day), and OC5 (days three to five) before arrival at Mt. Zeppelin. In this procedure missing data were flagged as such, and were not taken into account.

### 2.5 Ice data

For the interpretation of events of new particle formation observed during the *Oden* cruises information on pack ice extent under the air masses reaching the sampling points proved crucial (Heintzenberg et al., 2015). Another motivation for utilizing ice data in the present study is the fact that the Svalbard region experiences large seasonal changes in pack ice cover which we expect to have strong effects on emissions of particles and their precursor gases. Thus daily ice concentrations were taken from the NSIDC database (https://nsidc.org/data). The irregularly shaped data gap around the pole caused by the inclination of satellite orbits and instrument swath was filled with 100% cover. To each hourly position and data of the back trajectories the ice information in the corresponding maps of ice concentrations were added and displayed in Fig. 2. On average the closest pixel in the ice maps was about 12 km off any trajectory point.

In the discussion of results we utilize the complement of ice cover, i.e., the amount of open water because the marine biological processes of interest predominantly take place in the open water, (Leck and Persson, 1996a). As integral parameters average open water, (OW), percentages along each back trajectory were calculated and will be referred to as OW1 (the last day), OW2 (the last but one day), and OW5 (days three to five) before arrival at Mt.

386 Zeppelin. The most solid ice cover is seen in an area reaching from Northeastern edge of
387 Greenland via North Pole to Parry Island. A marginal ice zone extends along the east coast of
388 Greenland to Franz-Josef-Land, and the area between Svalbard and the latter island.
389
390
391 **2.6 ERA-Interim data of sea surface temperature**
392
393 Daily Sea Surface Temperature (SST) data for our study period (2006-2015) were
394 downloaded from the website of the European Centre for Medium-Range Weather Forecasts
395 (ECMWF). A description of the global atmospheric reanalysis, (ERA-Interim), has been
396 given by Dee et al. (2011), and a guide to the products and the download procedures can be
397 found at http://www.ecmwf.int/en/elibrary/8174-era-interim-archive-version-20. Briefly,
398 ERA-Interim is an assimilating model reanalysis of the global atmosphere and sea-surface
399 physical parameters covering the data-rich period since 1979. SST data were downloaded at a
400 resolution of approximately 0.56° and regridded onto the same 46 km equal-area sinusoidal
401 grid used for DMSP and cloud fraction, (see below). Ice-covered pixels were screened out
402 prior to the back-trajectory analysis. In the Arctic region, ERA-Interim has been shown to be
403 a top performer among a number of atmospheric reanalyses, (Lindsay et al., 2014).
404
405
406 **2.7 MODIS cloud fraction**
407
408 Persistent cloud cover limits PPP in Arctic and Sub-arctic seas, (Bélanger et al., 2013), and,
409 as mentioned above, irradiance at the sea surface, which is largely controlled by cloudiness,
410 influences $DMSP_{dissolved}$-to-$DMS_{aq}$ conversion. Boundary layer clouds are known to be
411 additional controllers of the surface aerosol (Heintzenberg, 2012). In the summer Arctic low

level clouds and fogs are widespread (Warren and Hahn, 2002). Both scavenging and new particle formation have been observed in connection with low clouds and fog passages (Lannefors et al., 1983; Heintzenberg and Leck, 1994; Leck and Bigg, 1999; Heintzenberg et al., 2006; Karl et al., 2013). Beyond the cloud base derived from the ceilometer we have no other in situ local or regional cloud information. Thus, we utilize satellite-derived cloud information.

Daily Level-3 global cloud fraction with one-degree resolution was downloaded from NASA website (http://modis-atmos.gsfc.nasa.gov, Hubanks et al., 2015) and extracted for our region of interest. Briefly, level 3 images correspond to the aggregation of all level 2 images (1 km resolution) available within the one-degree resolution grid. For a given L2 scene, each pixel is assigned a value of 1 (cloudy) or zero (clear sky), and then the individual scene values are averaged over a 24-hour period. Note that a given pixel can be revisited up to six or seven times in the course of a day at high latitudes. Finally, the daily composites were re-projected to 46.4 km pixels to match the spatial resolution of DMSPt. The average distance between a trajectory point and the closest MODIS pixel was 18 km.

The cloud fraction CF as well as other cloud properties from MODIS have been extensively used, for instance to study the global spatial and temporal distribution of clouds over the last decade (e.g., King et al., 2013). Several studies have also successfully performed validation by comparison with in situ data (e.g., An and Wang, 2015) which demonstrated the ability of the MODIS-aqua sensor to retrieve cloud cover.

Following the same approach as with the ice data and DMSPt, average cloud fractions, (CF, see Table 1), along each back trajectory were calculated and will be referred to as CF1 (the last day*)*, CF2 (the last but one day), and CF5 (days three to five) before arrival at Mt. Zeppelin. Missing data are flagged as was done with DMSPt data.

## 3. Three approaches to identifying events of new particle formation

There are no definitive and no generally accepted methods to identify or predict NPF-events in atmospheric time series of aerosol data. Thus, in the present study we explored different approaches with varying degrees of complexity to identify such events. We emphasize that none of these approaches explicitly is connected to diel cycles such as in Dal Maso et al., (2005) or makes any assumptions about the time of day during which new particle formation occurs. Three objective search algorithms were written in FORTRAN to analyze the time series of hourly records of aerosol parameters in search of new particle formation:

1. The simplest approach of upper percentiles (PCT-approach), assumes that NPF-events are characterized by extremely high concentrations of small particles in terms of N25 (see Table 1). The key parameter characterizing each PCT-event was the value of N25 averaged over a fixed number of hours, ($N25_{av}$), after the nominal start of an event, (see below). With $N25_{av}$ also a nominal length of PCT-events was defined as the number of hours after the start of an event by which N25 sank to less than half of $N25_{av}$.
2. The more specific approach of diameter growth (DGR-approach) builds on the temporal development of the particle size distribution in terms of a systematic growth of the diameter D50 (see section 4.1) to find the classical "Banana Type" of NPF-event, (Kulmala et al., 2004). The key parameter characterizing each DGR-event was the average growth of D50 during the nominal event length NUC, (see below). For this approach the nominal length of events was reached when the running two-hour average growth fell below the value one.
2. The most complex approach of multiple-size events, (MEV-approach), searches for events with concurrent appearance of concentration increases in several size classes below 60 nm diameter (Karl et al., 2013; Leck and Bigg, 2010). The key parameter characterizing each MEV-event was the relative concentration increase averaged over the chosen size classes

below 60 nm during the nominal event length NUC, (see below). As with PCT-events a nominal length of MEV-events was defined as the number of hours after the start of an event by which N25 sank to less than half of $N25_{av}$.

Three time-related parameters were commonly defined for all three approaches:

1. Nominal NPF-event length, (NUC) was nine hours.
2. Pre-event periods, (PRENUC), from which increases in diameters or number concentrations were calculated, were six hours.
3. Reference periods, (REF), before PRENUC and after NUC periods were defined in order to compare event and pre-event data with non-event conditions. Each of these reference periods had the length of half the sum of pre-event plus event time periods, making the total reference time period of each event as long as that of the event itself.

Besides these common characteristic lengths individual fixed thresholds were chosen and discussed below for each approach in order to generate at least 200 unique events per approach, (see Table 2).

The aerosol data used to define the NPF-events were complemented by a large number of environmental parameters. The primary temporal resolution of the environmental parameters was between one minute (C25, cf. Table 1) and five days (DMSPt, cf. Table 1). C25 was calculated as 25% percentile on an hourly basis. The parameters with resolutions higher than an hour (OW, CF, and OC, cf. Table 1) were evaluated along the hourly back trajectories. While this procedure yielded hourly varying results even of OW, CF, and OC it has to be kept in mind that this hourly variability is the result of hourly resolved trajectories traversing the grid; the low primary temporal resolutions of the OW, CF, OC, and chemical parameters remain. For these slowly varying parameters the REF periods before and after the events were extended to one day beyond the longest primary resolution, i.e., six days.

For two reasons the three search algorithms may yield temporarily redundant results, i.e., they may identify the same events. One, they go independently through the same time series of aerosol data, possibly causing inter-approach redundancy. Two, each algorithm goes through the time series hour by hour, thus allowing for temporal overlap of events found by each approach, (intra-approach redundancy).

The three types of events were assumed to be mutually exclusive and potentially being caused by different sets of conditions for new particle formation. Thus, a FORTRAN procedure was developed to eliminate both intra and inter-approach redundancy while maintaining a maximum of identified NPF-events. To remove intra-approach redundancy the procedure identifies overlapping events within each approach. Of each ensemble of such overlapping events the one with the strongest key parameter of the respective approach (growth of D50, or concentration increases as defined above) is retained. Next, inter-approach redundancy is addressed by the procedure. However, there is no unique solution to the problem of the partly redundant three time series of events. In order to avoid any preference of one or several types of events in the tests of inter-approach overlap pairs of events of different approaches are chosen at random and compared for overlap. This random comparison is done as often as the product of the number of events of the three approaches. This rather time-consuming random test yields stable numbers of non-overlapping events within less than one percent, irrespective of the order in which the events of the three approaches were arranged for the test. By removing intra and inter-approach redundancy in the first two steps of the procedure a number of time periods will be “freed”. Consequently, in a last step, the procedure tries to fill the “freed time periods” non-redundantly with events of the three approaches that had been eliminated in the first two steps. Table 2 collects total numbers and unique numbers of events for each approach. In the rest of the paper only non-redundant events will be discussed. The total number of new particle formation events will be shortened to TNPF.

### 3.1 The upper percentile of N25 (PCT-approach)

Events of new particle formation were identified by time periods in which N25 was consistently, i.e. on average for three hours, above a set threshold. With a threshold of the 93%-percentile (170 $cm^{-3}$) 4143 PCT-events were identified in the total data set, only 240 of which were unique because most of them overlapped with event or pre-event times of the other two approaches. Average N25 during these unique events was 330 $cm^{-3}$ and the average length of events 4 ±0.9 h, (one standard deviation).

Fig. 4, (top), shows the average temporal development of the relative size distributions for the unique PCT-events as in the results in Karl et al. (2013), i.e. relative concentrations were formed by dividing the absolute number concentrations by the average total number during the six-hour pre-event time periods. The events are characterized by a nearly monomodal distribution around 20 nm that broadens somewhat around the nominal start of the events. During the last three hours before the events D50 decreased slightly and returned to the pre-event level during the nine NUC hours.

In connection with PCT-events average aerosol parameters NTO through N300 showed an average increase by a factor of 2.2 during PRENUC-periods, which was maintained on an average level of 1.5 during the events. The aerosol-chemical parameters $Na^{+}$, $nssSO_4^{-2}$, and MSA were on an average level of 20% of their reference value. The average environmental parameters indicate a strong increase by a factor of 14 in solar radiation and a lifting of cloud base before the events. During the events the level of solar radiation was still elevated by a factor of six above its reference value. As a consequence temperature at the station was up by 2 – 3 degrees. Precipitation 12 h before trajectory arrival time, (SP12) was a factor of five above reference levels for air arriving during NUC-periods, whereas SP35 to SP5D were below their respective reference levels. Cloud fractions were slightly raised 12 - 48 h before air arrival. Of the ocean parameters more open water was met by trajectories 12 to 24 before

their arrival with ocean temperatures 12 to 48 h before trajectory arrival having been up to four degrees warmer than their respective reference values. On average DMSPt-parameters OC24 through OC5D showed were raised by a factor of two above their reference value.

In Fig. 5, (left top panel), average trajectory height profiles during PRENUC and NUC-periods are displayed. Widely varying vertical air mass paths occurred before and during PCT-events. Median vertical trajectory paths during PRENUC and NUC times indicated air coming from some 300 m above station level five days ago sinking to about one hundred meters above station level during the last two days before arrival. The upper quartiles of the PCT-height profiles point at strong subsidence before air mass arrival.

The right top panel in Fig. 5 maps average horizontal trajectory positions in 12 h steps in months having at least ten PCT-events, i.e., May - September. Filled circles around the trajectory positions comprise 95% of all events. The monthly average horizontal trajectory direction during PCT-events mostly was from the northwest. In June and July the trajectories reached farthest into the multiyear ice cover northeast of Greenland. Only during September the back trajectories covered ice-free and marginal ice areas in the Fram Strait. We note that the five-day back trajectories of PCT-events, (and of the other two approaches as well), stayed within some 800 km of Mt. Zeppelin.

### 3.2 The diameter growth (DGR) approach

The DGR-approach to identify events of new particle formation builds on the classical concept of particle growth through condensable vapors after an initial nucleation of sub-five nanometer particles that cannot be observed with the available instrumentation, so called "Banana-type" (Kulmala et al., 2004). The respective algorithm utilizes the parameter D50, (see Table 1), and requires a growth of this diameter by at least a factor of 1.5 after the

567 nominal start of an event. With this threshold the algorithm searched through all 87646 hours
568 of the ten-year record and found 1199 DGR-events of new particle formation. After
569 eliminating cases of temporal overlap with the other two approaches 235 unique events of this
570 type remained, (see Table 2). Other or more DGR-events could have been found by
571 shortening the nominal nine NUC hours. For two reasons we refrained from discussing
572 shorter growth periods in the DGR-approach. Maintaining common-length NUC periods
573 facilitated the comparison of results of the three approaches. Furthermore, reducing the
574 growth period would also make PCT and DGR-events ever more similar.

575 In the analysis of atmospheric data and theoretical modeling of NPF-events of type DGR
576 two key parameters are discussed, namely particle formation rate J ($cm^{-3}s^{-1}$) and growth rate
577 GR ($nmh^{-1}$) of particle diameters. For both parameters the measurement protocol by Kulmala
578 et al. (2012) provides specific calculation procedures, (equations. 2, 7, and 9), which we
579 follow in the present study, albeit with the caveat that the one-hour temporal resolution of our
580 time series is far below the ten-minute time resolution that the protocol of Kulmala et al.
581 (2012) requests in order to be able to follow the rapid development of NPF-events.
582 Furthermore, only the 127 DGR-events identified from 2011 on are based on particle size
583 distributions measured down to a diameter of five nanometers.

584 The sizes of newly nucleated aerosol particles are of order 1–2 nm, which is below or near
585 the limit of existing measurement techniques. When the nuclei grow in size their number
586 concentration decreases because of various removal mechanisms. Instead of particle
587 formation rates at the initial nucleus size so-called apparent nucleation rates Jx are often
588 reported, i.e. rates at which new particles appear at some larger observable particle diameter
589 dx. For the present study two apparent nucleation rates are calculated: DGR events of the
590 whole time series have been identified with particle size distributions measured at diameters
591 from 10 nm up through the growth of the number median diameter D50 in the size range 10 –
592 50 nm. Thus we calculated J22 for these 235 events at the nominal geometric mean diameter

593 of 22 nm. For 127 of these events size distributions reached down to five nanometer
594 diameter, (years 2011 and later). For these events we calculated J11 at the geometric mean
595 diameter 11 nm as representative for the diameter range 5 – 25 nm, which is close to the
596 frequently reported apparent formation rate J10 at 10 nm diameter. Additionally, the two
597 corresponding grow rates GR22 and GR11 were calculated in the respective diameter ranges.
598 Statistics of these four key parameters of the DGR events are collected in Table 3.
599 Depending on the pollution level at the measuring site widely varying values of J10 have been
600 reported. For the polluted subtropical environment of Taiwan Young et al. (2013) give values
601 from 4.4 to 30 $cm^{-3}s^{-1}$ whereas Pierce et al. (2014) published values between 0.22 and 0.84
602 $cm^{-3}s^{-1}$ from a rural Canadian setting. The latter range is within the range 0.1 – 9.4 $cm^{-3}s^{-1}$
603 with a median value of 1.2 $cm^{-3}s^{-1}$ reported by Yli-Juuti et al. (2009) for a station in rural
604 Hungary. The two formation rates of the present study cover the range 0.1 – 1.4 $cm^{-3}s^{-1}$ for
605 the 25% to 75% percentiles (see Table 3), which covers the range of 0.05 to 0.13 $cm^{-3}s^{-1}$ given
606 by Vencaz et al. (2009) for a remote site in the Himalaya. The environmental conditions at
607 the Siberian station Tiksi at the coast of the Laptev Sea may come closest to our Arctic
608 setting. From this site Asmi et al. (2016) published formation rates of 0.01 to 0.41 at an
609 unspecified particle size.
610 In terms of 25% to 75% percentiles the particle growth rates of the present study range
611 from 0.4 to 1.4 $nmh^{-1}$ in the range 5 – 25 nm and 1.0 to 1.8 $nmh^{-1}$ in the diameter range 10 -
612 50 nm, which is near the range of results of 1 – 2 $nmh^{-1}$ derived by Ström et al. (2009) for
613 new particle formation in the lower boundary over Ny-Ålesund, Spitsbergen but considerably
614 lower than the maximum growth rate of 3.6 $nmh^{-1}$ reported by Asmi et al. (2016) for July at
615 the Siberian station Tiksi at the coast of the Laptev Sea. For open ocean new particle
616 formation events over the North Atlantic O'Dowd at al. (2010) report a "typical growth rate"
617 of 0.8 $nmh^{-1,}$ whereas Ehn et al. (2010) give an average growth rate of 3 $nmh^{-1}$. We note that
618 the average length of DGR-events was 10 ±1 h, (one standard deviation). Further details

about the connection between growth rates and the two formation rates can be found in the supplement.

The average temporal development of the relative number size distribution during DGR-events is presented in Fig. 4, (center). After a decrease of the sub-50 nm diameter median from about 25 to 16 nm during the six hours before the nominal start of the events D50 increases systematically during the following nine NUC hours with somewhat reduced growth towards the end of the event.

During the PRENUC-periods particle number concentrations N300, and the condensation sink, (CS), decreased relative to the reference periods before and after the events. Subsequently, during the NUC periods the strongest increases was found for N60. Environmental parameters around air mass arrival showed a strong lifting of cloud base, (C25), and an extremely high increase in solar radiation, (by a factor of 11 during PRENUC and by a factor of 60 during NUC periods). However, 12 h before air arrival precipitation had been up by a factor of 2.5. Cloud fractions were down to about 70% of their reference values 24through 48 h before air arrival. Of the chemical aerosol parameters $Na^{+}$ and $nssSO_4^{-2}$ showed an increase of 2.6 and 2.3, respectively. OC12 and OC48 were slightly higher than reference level before and during the events. Sea surface temperatures T24 were raised by nearly one degree whereas earlier SST-values, (T36 – T5D), were up to one degree below reference values.

Fig. 5, (left center panel), shows statistics of the vertical air movement before trajectory arrival during DGR-events at Mt. Zeppelin covering a wide range of vertical movements between 200 m and beyond 1500 m height. During the days when elevated DMSPt levels were noted median trajectory heights were six to nine hundred meters. Median trajectories during PRENUC times dipped down to the station level, (474 m a.s.l), about one day before arrival, albeit lifted and subsided again shortly before arrival. Vertical trajectory pathways will be discussed further in Section 4.2.

645 Monthly average trajectory positions and their variability in connection with DGR-events
646 are shown in Fig. 5, (center right panel). The months April through October had at least ten
647 DGR-events per month. As with PCT-events the general trajectory direction was from the
648 northwest, mostly staying for several days over the marginal ice zone between northeastern
649 Greenland and eastern Svalbard. During the earliest month of April with 14 DGR-events the
650 back trajectories reached farthest south into the ice-free parts of the Fram Strait.
651
652
653 **3.3 The Multiple-size approach (MEV)**
654
655 Leck and Bigg (2010) and Karl et al. (2013; 2012) discussed a type of new particle formation
656 that to date only has been reported from the summer Arctic. During these MEV-events high
657 ultrafine particle concentrations appear concurrently in a broad diameter range reaching from
658 under 10 to some 60 nm. We simulated this type in a search that required the concurrent
659 increase of NTO, N20, N40, and N60, (cf. Table 1), as averaged over the first three NUC
660 hours by a factor $\geq 1.6$ over their respective averages during the six (PRENUC) hours. Over
661 the ten years of data 1191 such events of this type were identified, 266 of which remained
662 after removal of those overlapping with events of other approaches. During these unique
663 events the average concurrent concentration increase was 4.7 and the average length of the
664 events 12±0.8 h.
665 The concurrent appearance of high concentrations at many particle sizes below 60 nm
666 resembles the nocturnal NPF-events analyzed by Suni et al. (2008) in the Australian
667 Eucalyptus forest and simulated in subsequent chamber experiments (Ristovski et al., 2010;
668 Junninen et al., 2008). We emphasize though that the condensing vapors in the Australian
669 NPF-events originating from terrestrial biogenic emission are quite different from the

polymer gels implicated in the Arctic MEV-events and originating from the surface microlayer of the ocean.

The bottom part of Fig. 4 shows the average temporal development of relative number size distributions before and during MEV-events. The development before the nominal start of MEV-events is more complex than during the PRENUC-periods of the first two types of events. Intermittently a mode around seven nanometers shows up that broadens and becomes more prominent about two hours before the nominal start of events. The major PRENUC-mode around 25 nm also broadens and becomes more prominent towards NUC. A weak mode exists during PRENUC around 120 nm and hardly any particles beyond 400 nm. D50 sinks from 25 to about 20 nm and stays below 25 nm through the MEV-events even though number concentrations increase during the first NUC-hours by more than a factor of five.

During NUC-periods all particle number concentrations increased, on average by a factor of 1.6. Average solar radiation also increased by about 90% above reference level during NUC-periods. Of the chemical parameters $nssSO_4^{-2}$ showed an increase by a factor of three during PRENUC and NUC-periods, and MSA a slight increase during PRENUC-periods. On one hand, precipitation 12 h, and 36 to 48 h before trajectory arrival, (SP12, SP48), were above reference levels for air arriving during PRENUC-periods. On the other hand, during PRE, SP24, SP36, an SP5D indicated dry conditions during PRENUC and NUC-periods. Only three to five days before air arrival slightly increased cloud fractions were noted. Sea surface temperatures up to five days before trajectory arrival were on average about one degree lower than their reference values. DMSPt parameters OC12 to OC36 were raised by factors of 1.3 and 1.6 during PRENUC and NUC-periods, respectively.

Percentiles of vertical trajectory coordinates prior to and during MEV-events are displayed in Fig. 5, (bottom left panel). During the events, and even stronger during the PRENUC periods median trajectories had been below 500 m for more than four days. Furthermore, the final air approach to Mt. Zeppelin mostly came from below the station level. Upper quartiles

696 of the vertical trajectory positions are substantially lower than with DGR-events. We note,
697 however, that a short excursion above station level occurred in the upper quartiles during the
698 last three hours before arrival.

699 The bottom right panel of Fig. 5 gives the monthly average trajectory positions and their
700 variability in connection with MEV-events. The months April through October had at least
701 ten MEV-events per month. As with the other approaches the general trajectory direction was
702 from the northwest, albeit with stronger swings towards the ice-free areas south of Svalbard
703 early and late in the season, (April, May, and September). Interestingly, the trajectories of the
704 11 MEV-events in October were directed nearly straight north from the North Pole.

705 Summarizing differences and commonalities among the results of the three approaches we
706 can state that the length of the events increases from four to ten and twelve, going from PCT
707 to MEV-events. PCT-events are characterized by lower-than-reference aerosol-chemical
708 parameters. $Na^{+}$ and $nssSO_4^{-2}$ show strong increases in the other two types of events: $Na^{+}$ in
709 connection with DGR-events and $nssSO_4^{-2}$ in connection with MEV-events. Both, PCT and
710 DGR-events exhibit strong increases in solar radiation. Precipitation before air arrival was
711 raised at varying times in connection with the three types of events. Cloudiness both
712 increased and decreased at varying times before air arrival with the three types of events.
713 Increased open water under the trajectories was strongest with DGR-events and least
714 important with MEV-events. Only in connection with PCT-events strongly raised sea surface
715 temperature were noted before trajectory arrival. DMSPt related ocean parameters were
716 raised to varying degrees and at varying times before all NPF-events, most strongly in
717 connection with PCT-events and least in connection with DGR-events.

718

719

720 **4. Discussion**

721

### 4.1. Environmental setting

The discussion of the results on new particle formation in the Svalbard region builds on the variability of new particle formation and related environmental parameters on scales of months, and days. Fig. 1 gives an overview over the geographic areas which were covered by one, two, and five-day back trajectories to Mt. Zeppelin during the ten years of the present study covering the months March through October. This figure illustrates that air arriving at Mt. Zeppelin during the ten summers of the present study came from widely varying regions from the central ice-covered Arctic via the northern seas and northernmost Scandinavia to Greenland. One-day back trajectories cover a roundish area from the central east coast of Greenland via northern Scandinavia to Franz-Josef-Land, North Pole and back to the north coast of Greenland. Excluding inner Greenland this area is widened by roughly 500 km by 2-day back trajectories and by at least another 500 km by 5-day back trajectories reaching over most of Greenland and the adjacent seas west of Greenland. This is a much wider region from which air may reach Mt. Zeppelin as compared to sites in the inner Arctic as illustrated in Fig. 2 of Heintzenberg et al. (2015).

On the path of trajectories to Mt. Zeppelin quite different ice conditions were met (see, Fig. 2). On average North Atlantic open waters reached around West Spitsbergen all the way to Nordaustlandet. Drift ice was passed over by trajectories along the whole east coast of Greenland. One-day trajectories passed over the marginal ice zone from the Fram Strait to Franz-Josef Land but also over more contiguous ice close to the North Pole. At times, with five-day back trajectories, even the marginal ice regions of Baffin Bay and Beaufort Sea were reached.

The long-term geographical distribution of DMSPt in Fig. 3 reflects the water conditions for phytoplankton biomass around Svalbard. Directly at the coasts of Greenland and Eurasia increased nutrient availability in coastal and shelf waters (due to continental run-off and

748 enhanced hydrodynamics) cause localized areas of high DMSPt values. The low DMSPt
749 values further out along the coast of Greenland are due to sea ice reaching through the Fram
750 Strait far south, (see Fig. 2). A prominent feature in the regional DMSPt distribution is the
751 tongue of high DMSPt, (intense blue color), and thus high phytoplankton biomass east of this
752 area, reaching from Spitsbergen to roughly Jan Mayen that lies within one-day back
753 trajectories. Northward-flowing Atlantic waters, carried by the West Spitsbergen Current,
754 and southward-flowing fresh surface waters from melting ice, and recirculated Atlantic
755 waters, carried by the East Greenland Current (Rudels et al., 2005) are meeting. The layering
756 created by water masses of different density stabilizes the water column and traps
757 phytoplankton cells at well-lit depths. If sufficient nutrients are available, this can lead to the
758 development of large phytoplankton blooms, which can result in high concentrations of
759 $DMS_{aq}$, (see Fig. 2 in Leck and Persson, 1996a).
760 In the ten-year average cloud fractions systematic differences in cloudiness appear.
761 Depending on transport pathways as identified by the back trajectories, cloudiness varies on
762 the way to Spitsbergen. The ice-covered areas, (cf. Fig. 2), from the east coast of Greenland
763 to Franz-Josef-Land exhibit somewhat lower cloud fractions than the ice-free regions
764 southwest to east of Spitsbergen.
765
766
767 **4.2 Seasonal variability**
768
769 Seasonal changes are discussed in terms of monthly averages taken over the ten-year study
770 period. As expected in Earth's polar regions the seasonal variability of all environmental
771 parameters is very high as exemplified by the solar flux, (SFL), and the air temperature,
772 (TEM), at Mt. Zeppelin in Fig. 6. Due to the seasonal change in cloudiness, (cf. Fig. 7), the
773 seasonal distribution of SFL is not quite symmetrical about midsummer but is skewed slightly

774 towards the cloud minimum in spring. The air temperature, however, does not peak before
775 July and has a broad shoulder into fall and winter. The first, and partly absolute maxima, of
776 the seasonal distributions of NPF-events in Fig. 6 coincide with that of the SFL but then drop
777 of more slowly towards fall than solar radiation. In particular, MEV-events do so and even
778 have their main maximum in August. The occurrence of all NPF-events drops off sharply in
779 October. Whereas May as the first month with larger numbers of events is dominated by
780 PCT-events, followed by DGR and then MEV-events, the contributions of the three NPF-
781 types are reversed in the last month with high NPF-numbers, i.e., September.

782 Fig. 6 clearly shows that the formation of new particles in the Svalbard region is not
783 controlled by the late winter-to-early-spring phenomenon of Arctic haze peaking with highest
784 sulfate-concentrations in March, (cf. Fig. 3 in Heintzenberg, 1989, and Fig. 6), which has a
785 minimum in the total number of NPF-events. This minimum is in contrast with the maximum
786 in new particle formation rates found by Croft et al. (2016a) with their global aerosol model.
787 The high numbers of accumulation mode particles during the Arctic haze months in late
788 winter and spring yield the annual maximum in condensation sink, (CS in Fig. 6), which
789 could quench nucleation events and subsequent growth. Thus, even though photochemistry
790 may produce significant amounts of nucleating material, the freshly formed particles will not
791 grow to stable size before they are removed via either deposition or coagulation as discussed
792 by Tunved et al. (2013) and others. An alternative explanation of the late onset of NPF-
793 events in TNPF in spring lies in the marine biological processes not being activated nearby
794 during the Arctic haze period yet, (Heintzenberg and Leck, 1994).

795 Fig. 7 collects the seasonal variation of environmental parameters as averaged along the
796 back trajectories to Mt. Zeppelin. From their minimum in March-April open water conditions
797 improve until September, after which the pack ice extent under the trajectories rapidly
798 increases again. The widening open water areas are reflected in sea surface temperatures
799 under the trajectories that increase until September before they drop off strongly in October.

800 Consequently, because of its connection to marine biological activity DMSPt increases in the
801 euphotic zone from first photosynthetic light in May until it evens out around July and drops
802 off in October. Largest DMSPt values are reached in the vicinity of Svalbard, (cf. OC12 in
803 July and August in Fig. 7), i.e. considerably later than MSA. The ending of DMSPt-curves in
804 October is due to the lack of data not due to zero-DMSPt. Still, DMSPt concentrations are
805 expected to be low at this time of the year at temperate to polar latitudes due to low
806 phytoplankton biomass and low light exposure, (see Fig. 9 in Galí et al., 2015). In terms of
807 the MODIS-derived cloud fraction cloudiness increases rapidly from its minimum in April
808 and evens out on a plateau of 80 – 90% after July. The spring-minimum in cloudiness is
809 confirmed by the maximum in cloud base as indicated by C25 in Fig. 7. This seasonal
810 distribution of cloudiness does not correspond to the classical picture of near-surface
811 cloudiness that exhibits near cloud-free conditions in winter and mostly overcast with Arctic
812 stratus and fogs during the summer months (Warren and Hahn, 2002; Huschke, 1969). We
813 explain the difference by the specific atmospheric pathways covered by the back trajectories
814 of the present study (cf. Fig. 1). Trajectory-averaged precipitation parameters (SP12-5D in
815 Fig. 7) have minima in the period April – May, from which they increase towards their
816 maxima in fall and winter.
817 The chemical aerosol information derived from the analyses of filters samples has a
818 relatively low temporal resolution of at least one day combined with frequent gaps of several
819 days in between samples. Thus, it cannot directly be related to the time periods of NPF-
820 events. The seasonal distribution of chemical tracers, however, yields important information
821 about new particle formation. Taken over the whole year $nssSO_4^{2-}$ in Fig. 6 is largely
822 anthropogenic, (Heintzenberg and Leck, 1994), and has its maximum during the peak of
823 Arctic haze in March and April and its minimum in August, which does not match any
824 seasonal distribution of NPF-events. We also plotted $Na^+$ in Fig. 6 as a tracer of the inorganic
825 marine aerosol components sea salt. $Na^+$ decreases from its winter maximum to its summer

826 minimum in June/July, again without similarity to the NPF-distributions. Instead, the
827 seasonal distribution of $Na^+$ rather closely follows that of the trajectory-derived wind speed
828 during the last hour before arrival, (not shown in the figure). Wind speed as driver for sea salt
829 production is a well established phenomenon (Blanchard and Woodcock, 1957). After a steep
830 rise in April MSA in Fig. 6 sharply peaks in May and then gradually drops off towards its
831 minimum in October, more gradually than reported for data taken from 1991 to 2004 by
832 Sharma et al. (2012) and earlier than reported by Heintzenberg and Leck (1994), both at the
833 same station. Our seasonal distribution of MSA most closely resembles that of SFL, in Fig. 6,
834 albeit with its peak in May a month earlier that SFL and more strongly skewed towards
835 spring. According to Leck and Persson (1996b) on average the concentrations of the marine
836 biogenic sulfur components, (DMS and MSA), fell with a decline rate of about 30% per week
837 approaching zero values in September explained by reduced ppp (Leck and Persson, (1996a),
838 (consistent with Becagli et al., 2016).

839 As MSA is the only measured aerosol component with exclusively marine biogenic
840 sources, we illustrate its seasonal distribution in greater detail in Fig. 8. In this figure MSA-
841 concentrations measured on Mt. Zeppelin have been extrapolated along 5-day back
842 trajectories, forming monthly average monthly maps of potential MSA-sources during the
843 biologically most active months of March through October.

844 Fig. 8 yields several pieces of information that are relevant to the issue of new particle
845 formation. Early in spring the biological aerosol sources are limited to the North Atlantic and
846 Norwegian Sea. In April the tongue of newly opened waters between Novaya Zemlya and
847 Franz-Josef-Land seemingly is beginning to become biologically active. In May this area
848 widens towards the Barents Sea while the North Atlantic also becomes more active, reaching
849 the Fram Strait. In August two wide potential source regions cover the region from Northern
850 Greenland to the northern end of Scandinavia and the region Barents to Kara Sea. In
851 September even the pack ice north of Svalbard becomes biologically active, (Leck and

852 Persson, 1996a), and shows potential MSA sources, in particular, north of the northern coast
853 of Greenland. Finally, the very weak potential MSA sources in October appear to be situated
854 mainly over the Kara Sea and over the North Atlantic.

855 How do these seasonal distributions compare to those of the NPF-events identified by the
856 three search-approaches defined in Section 3? To address this question we constrained the
857 average seasonal distribution of environmental parameters to those hours that had been
858 identified by the NPF-events of the three approaches. However, none of the individual
859 seasonal distributions of constrained environmental parameters follows closely any of the
860 NPF-events. In particular, the main MSA peak remains in May, thus one month earlier than
861 any peak of the NPF-occurrences. To elucidate further potential differences in the three types
862 of NPF-events we return to the discussion of vertical pathways of related back trajectories,
863 (see Fig. 5). In this figure all three types of NPF-events exhibit a wide range of vertical
864 trajectory paths. As we expect the regional sources of primary particles and particle
865 precursors to be at or near the surface we segregated the NPF-events into subpopulations with
866 back trajectories that remained a given time below 500 m, (roughly station level). In Fig. 9
867 we collected the results concerning the 93 NPF-events that occurred with trajectories under
868 the 500 m limit, i.e., roughly 12% of all events. The top panel shows that the related
869 trajectories not only stayed below 500 m through most of the last five days before arrival but
870 close to the surface until they started rising to the station level about 24 h before arrival. The
871 peak of the sum of event occurrences now coincided with the main MSA peak in May, (see
872 center panel in Fig. 9). For DGR-events the May-maximum was particularly strong whereas
873 the PCT-predominantly occurred in May and June and MEV-events remained clustered
874 around the later part of summer, possibly coupled to SST and DMSPt.

875 A number of environmental parameters indicated substantial deviations from their
876 respective reference values during the months with most frequent occurrence of this sub-
877 population of NPF-events. Strongest deviations were noted for precipitation that was elevated

878 above reference levels two to five days before trajectory arrival, most prominently for DGR-
879 events in May, (by a factor of six 36 h before trajectory arrival). Strong positive deviations in
880 aerosol-chemical parameters only occurred with $Na^+$ in PCT and MEV-events, indicating
881 relatively high wind speeds near sea surface in the related air masses. MSA was elevated up
882 to 50% above reference levels only during MEV-events. Elevated levels of DMSPt were
883 noted with all three types of NPF-formation, most prominently for DGR-events 12 to 36
884 hours before which DMSPt was increased by a factor up to 1.7 relative to reference levels.
885 The bottom panel of Fig. 9 gives average trajectory positions in 12 h steps for the months
886 May through September. The circles around the steps comprise 95% of all trajectories.
887 During all months the trajectories stayed in the ice-free and marginal ice zone between Fram
888 Strait and Eastern Svalbard as illustrated by average July ice cover for the ten study years,
889 (for average monthly ice covers cf. Fig. 8). In particular during the earliest and latest months
890 of May and September the trajectories swing farthest south over the open water south of
891 Svalbard. We note that the complementary sub-population of results with trajectories
892 remaining above station level did not yield results that differed strongly from those for the
893 whole population of back trajectories.
894 As a last step in the discussion of seasonal variations in new particle formation a model is
895 formulated that describes the average sum of NPF-events, (TNPF), as a function of three
896 parameters, two of which are directly measurable at the site. With the linear combination of
897 the solar flux, (SFL, $Wm^{-2}$), average sea surface temperature under back trajectories 36 to 48
898 hours before their arrival at the site, (T48, °C), and condensation sink, (CS, $10^5$ $s^{-1}$):
899
900 $$TNPF = 0.57 \cdot SFL + 15.4 \cdot T48 - 0.69 \cdot CS$$
901

902 TNPF as shown in Fig. 10, can be described within an average deviation of 5% taken over the
903 major months with new particle formation, April - October. Any other of the sea surface
904 parameters describes TNPF less satisfactorily.

905 **4.3 Diurnal variability**

906

907 Average hourly occurrence of the three types of NPF-events is plotted in Fig. 11, (top). The
908 three approaches yield rather similar diel variations. From their minimum during the night
909 and early morning hours they reach their maximum occurrence between 12 and 16 h UTC in
910 the afternoon. One might expect the differences between the NPF-types to be due to the
911 requirement of the three types of NPF formation being mutually exclusive. However, this
912 constraint does not exclude that they occur at the same time of day, only that they occur at the
913 same time on the same day.

914 Over the continents new particle formation and growth events of the classical "Banana-
915 type" usually exhibit an increase in measurable precursors such as sulfuric acid shortly after
916 sunrise followed by the detection of increased numbers of nanometer-sized particles between
917 one and two hours later (Kulmala et al., 2004), who deduce a connection to photochemically
918 produced condensable vapors from this daily pattern. In the Svalbard region the sun is up all
919 day between mid-April and the end of August. Consequently we would expect the
920 photochemical production of condensable vapors to have a smaller diurnal amplitude than at
921 lower latitudes, which in turn should even out the diurnal pattern of NPF-events to some
922 degree. Despite the relatively small daily variations in solar elevations the solar flux on Mt.
923 Zeppelin varied on average by more than a factor of five during the sunlit days (see curve
924 SFL in Fig. 11, bottom). The daily maximum of SFL between 12 and 15 UTC coincides well
925 with the average diel change in N25 and NPF-occurrence. As expected in particle growth due
926 to condensable vapors after initial nucleation the daily maximum in N10 precedes that of N25
927 by a few hours.

928 The other process controlling the development of newly formed small particles is the
929 diurnal development of the planetary boundary layer, (Kulmala et al., 2004). We have no
930 data on the daily variation in boundary layer structure over or near the measurement site. The
931 ceilometer data yield the only high-resolution information with some connection to the
932 structure of the planetary boundary layer. During the summer months these data show a
933 consistent daily variation with a jump in most frequent hourly cloud base by about 100 m
934 from about 1570 m after 09 UTC with rather stable values following until 16 UTC, after
935 which cloud base decreases again to values comparable to the early morning hours. The
936 hourly medians of the vertical displacement parameter DZ, (see Fig. 11, bottom), provide a
937 clearer diurnal variation. While being negative throughout the day, i.e. indicating subsiding
938 air during the last hour before arrival at Mt. Zeppelin, DZ indicates the weakest subsidence in
939 early afternoon. We interpret diurnal variation in cloud base and DZ as indicative of local
940 clearing and convection during the day that may be conducive to photochemical processes
941 and mixing in the boundary layer, both of which would be enhancing new particle formation.
942
943
944 **5. Summary and conclusions**
945
946 Three different types of events of new particle formation, (NPF), were identified through
947 objective search algorithms formulated for the present study. The first and simplest algorithm
948 utilizes short-term increases in particle concentrations below 25 nm, (PCT-events). The
949 second one builds on the growth of the sub-50 nm diameter-median, (DGR-events), and is
950 most closely related to the classical "banana-type" of events, (Kulmala et al., 2004) involving
951 the presence of photochemically generated DMS oxidation precursors. The third and most
952 complex, so-called multiple-size approach to identifying NPF-events builds on the hypothesis

953 of Leck and Bigg (2010), suggesting the concurrent production of polymer gel particles at
954 several sizes below about 60 nm, (MEV-events).
955 In this analysis the possibility that sporadic anthropogenic emissions were interpreted as
956 NPF events cannot be excluded completely. However, there are a number of facts arguing
957 strongly against this possibility leading to serious misinterpretation of the data:
958 a) Location and operation of the Mt. Zeppelin station exclude local contamination to a very
959 large extent.
960 b) Manual inspection of the time series by one of the co-authors (PT) further reduced the risk
961 of contaminated data.
962 c) The temporal evolution of MEV events, i.e. concurrent and sustained concentration
963 increases at several particle sizes below 60 nm does not correspond to a typical passage of
964 stack emissions from a large combustion source, (Ogren and Heintzenberg, 1990). Instead, it
965 looks very much like MEV events observed under even stricter constraints on local or
966 regional sources of contamination on icebreaker Oden in the central pack ice area, (Karl et al.,
967 2013), and also looks similar to nocturnal NPF-events in Australian forests, (Suni et al., 2008;
968 Junninen et al., 2008).
969 With these algorithms NPF-events were identified in a ten-year record of hourly number-
970 size distributions taken at the research station on Mt. Zeppelin, Spitsbergen. As a first and
971 general conclusion we can state that NPF-events are a summer phenomenon and not related to
972 Arctic haze, which is a late winter-to-early spring event. The seasonal distribution of the
973 available information on cloudiness does not suggest any direct connection with NPF-
974 formation. The MODIS derived cloud fraction generally is very high (70 – 90%) and rather
975 evenly distributed over the Svalbard region during the months with high frequencies of NPF-
976 events. As already reported in Tunved et al. (2013) NPF-events appear to be somewhat
977 sensitive to the available data on precipitation derived from the trajectory model, in particular
978 when constrained to cases with back trajectories staying below 500 m. In this subpopulation

of NPF-events DGR-events show the strongest change in precipitation parameters in connection with new particle formation.

The seasonal distribution of solar flux suggests some photochemical control that may affect marine biological processes generating particle precursors and/or atmospheric photochemical processes that generate condensable vapors from precursor gases. Whereas the seasonal distribution of the biogenic MSA follows that of the solar flux it peaks before the maxima in NPF-occurrence. For PCT-events, and more distinctly so for DGR-events, this one-month delay disappears in the subpopulation with back trajectories staying below 500 m. MEV-events, however, maintain their peak occurrence later in summer and early fall.

With the limited information on particle size, composition, particle precursors, and environmental conditions no definitive statements can be made about the processes leading to the formation of new particles in the Svalbard region. A host of findings, however, point to varying and rather complex marine biological source processes. The potential source regions for all types of new particle formation appear to be restricted to the marginal ice and open water areas between Northeastern Greenland and Eastern Svalbard. During earliest and latest months with high numbers of NPF-events the back trajectories reach farther south into the open waters of the North Atlantic. Depending on conditions yet to be clarified new particle formation may become visible as short bursts of particles around 20 nm, (PCT-events), longer events involving condensation growth, (DGR-events), or extended events with elevated concentrations of particles at several sizes below 100 nm, (MEV-events). The seasonal distribution of NPF-events peaks later than that of MSA and, DGR and in particular of MEV-events reach into late summer and early fall with much open, warm, and DMSPt-rich waters around Svalbard, promoting the production of *Phaeocystis pouchetii* together with polymer gels. Consequently, a simple model to describe the seasonal distribution of the total number of NPF-events can be based on solar flux, and sea surface temperature, representing environmental conditions for marine biological activity, and condensation sink, controlling

1005 the balance between new particle nucleation and their condensational growth. Based on the
1006 sparse knowledge about the seasonal cycle of gel-forming marine microorganisms and their
1007 controlling factors we hypothesize that the seasonal distribution of DGR and more so MEV-
1008 events reflect the seasonal cycle of the gel-forming phytoplankton.

1009 Despite the rather small diel changes expected during the summer Arctic there is a
1010 significant diurnal variation in aerosol and environmental parameters. Diurnal distributions
1011 of particle numbers below ten, (N10), and below 25 nm, (N25) follow that of the solar flux
1012 rather closely with a maximum between 14 and 16 UTC with the maximum of N10 occurring
1013 a few hours before that of N25. This delay in maxima may be caused by a slow particle
1014 growth due to photochemically produced condensable vapors. With a peak around noon
1015 MEV-events show the earliest daily peak occurrence with PCT and DGR-events peaking
1016 between 15 and 17 h, more closely to the maximum solar flux. Considering the diurnal
1017 variation in vertical trajectory displacement, (DZ), the early daily maximum in MEV-
1018 occurrence may be simply controlled by boundary layer dynamics.

1019 With the large database of ten years of aerosol data on Mt. Zeppelin enriched by
1020 environmental atmospheric and marine data occurrences, pathways and potential source areas
1021 of different types of new particle formation in the Svalbard region were elucidated by the
1022 present study. More process related information about new particle formation would require
1023 dedicated mechanistic experiments with more detailed information on particle precursors,
1024 ultrafine particles, and boundary layer mixing processes. DGR and MEV-types of new
1025 particle formation seem to be more closely related to near-surface processes. Thus, a low-
1026 level site such as the reopened Station Nord, (Nguyen et al., 2016), would be more suitable
1027 for related mechanistic experiments. Station Nord has the additional advantage of being close
1028 to the potential source regions of DGR and MEV-events identified by the present study.

1029 Acknowledgements

1030

The back trajectories created through the local use of the HYSPLIT4 model developed, maintained and generously distributed by the Air Resources Laboratory of NOAA were a backbone of the present study. We are very grateful for the ceilometer data provided by the Alfred-Wegener- Institute in Bremerhaven/Potsdam and to NSIDC for their providing daily Arctic sea ice data. Complementing our own chemical analyses of Mt. Zeppelin filter data, sodium and sulfate results were taken from the EBAS database at the Norwegian Institute for Air Research (http://ebas.nilu.no), for which we are indebted to Anne-Gunn Hjellbrekke and Wenche Aas. We thank the NASA Ocean Biology Distributed Active Archive Center (OB.DAAC) for access to MODIS datasets. We are indebted to Yafang Cheng and Zhibin Wang for providing the algorithm for calculating the condensation sink. MG acknowledges the receipt of a Beatriu de Pinós post-doctoral fellowship funded by the Generalitat de Catalunya. Long-term funding oft he DMPS measurements was provided by the Swedish Environmental Protection Agency (Naturvårdsverket). We also thank Norwegian Polar Institute for substantial support oft the field operation on Mt. Zeppelin.

1047 Literature
1048
1049 Agarwal, J. K., and Sem, G. J.: Continuous flow, single-particle-counting condensation
1050 nucleus counter, J. Aerosol Sci., 11, 343-357, 1980.
1051 An, N., and Wang, K.: A Comparison of MODIS-Derived Cloud Fraction with Surface
1052 Observations at Five SURFRAD Sites, J. Appl. Meteor. Clim., 54, 1009-1020, 2015.
1053 Asmi, E., Kondratyev, V., Brus, D., Laurila, T., Lihavainen, H., Backman, J., Vakkari, V.,
1054 Aurela, M., Hatakka, J., Viisanen, Y., Uttal, T., Ivakhov, V., and Makshtas, A.:
1055 Aerosol size distribution seasonal characteristics measured in Tiksi, Russian Arctic,
1056 Atmos. Chem. Phys., 16, 1271-1287, 10.5194/acp-16-1271-2016, 2016.
1057 Ayers, G. P., Cainey, J. M., Granek, H., and Leck, C.: Dimethylsulfide oxidation and the ratio
1058 of methansulfonate to non sea-salt sulfate in the marine aerosol, J. Atmos. Chem., 25,
1059 307-325, 1996.
1060 Bates, T. S., Johnson, J. E., Quinn, P. K., Goldan, P. D., Kuster, W. C., Covert, D. C., and
1061 Hahn, C. J.: The biogeochemical sulfur cycle in the marine boundary layer over the
1062 Northeast Pacific Ocean, J. Atmos. Chem., 10, 59-81, 1990.
1063 Becagli, S., Lazzara, L., Marchese, C., Dayan, U., Ascanius, S. E., Cacciani, M., Caiazzo, L.,
1064 Di Biagio, C., Di Iorio, T., di Sarra, A., Eriksen, P., Fani, F., Giardi, F., Meloni, D.,
1065 Muscari, G., Pace, G., Severi, M., Traversi, R., and Udisti, R.: Relationships linking
1066 primary production, sea ice melting, and biogenic aerosol in the Arctic, Atmos.
1067 Environ., 136, 1-15, http://dx.doi.org/10.1016/j.atmosenv.2016.04.002, 2016.
1068 Beine, H. J., Argentini, S., Maurizi, A., Mastrantonio, G., and Viola, A.: The local wind field
1069 at Ny-Ålesund and the Zeppelin mountain at Svalbard, Meteorol. Atmos. Phys., 78,
1070 107–113, 2001.
1071 Bélanger, S., Babin, M., and Tremblay, J.-É.: Increasing cloudiness in Arctic damps the
1072 increase in phytoplankton primary production due to sea ice receding, Biogeosciences,
1073 doi:10.5194/bg-5110-4087-2013, 2013.
1074 Blanchard, D. C., and Woodcock, A. H.: Bubble formation and modification in the sea and its
1075 meteorological significance, Tellus, 9, 145-158, 1957.
1076 Browse, J., Carslaw, K. S., Mann, G. W., Birch, C. E., Arnold, S. R., and Leck, C.: The
1077 complex response of Arctic aerosol to sea-ice retreat, Atmos. Chem. Phys., 14, 7543-
1078 7557, 10.5194/acp-14-7543-2014, 2014.
1079 Charlson, R. J., Lovelock, J. E., Andreae, M. O., and Warren, S. G.: Oceanic phytoplankton,
1080 atmospheric sulphur, cloud albedo and climate, Nature, 326, 655-661, 1987.

Croft, B., Martin, R. V., Leaitch, W. R., Tunved, P., Breider, T. J., D'Andrea, S. D., and Pierce, J. R.: Processes controlling the annual cycle of Arctic aerosol number and size distributions, Atmos. Chem. Phys., 16, 3665-3682, 10.5194/acp-16-3665-2016, 2016a.

Croft, B., Wentworth, G. R., Martin, R. V., Leaitch, W. R., Murphy, J. G., Murphy, B. N., Kodros, J. K., Abbatt, J. P. D., and Pierce, J. R.: Contribution of Arctic seabird-colony ammonia to atmospheric particles and cloud-albedo radiative effect, Nature Communications, 7, 13444, 10.1038/ncomms13444

http://www.nature.com/articles/ncomms13444 - supplementary-information, 2016b.

Dal Maso, M., Kulmala, M., Riipinen, I., Wagner, R., Hussein, T., Aalto, P. P., and Lehtinen, K. E. J.: Formation and growth of fresh atmospheric aerosols: eight years of aerosol size distribution data from SMEAR II, Hyytiälä, Finland, Bor. Env. Res., 10, 323-336, 2005.

Das, R., Granat, L., Leck, C., Praveen, P. S., and Rodhe, H.: Chemical composition of rainwater at Maldives Climate Observatory at Hanimaadhoo (MCOH), Atmos. Chem. Phys., 11, 3743-3755, 10.5194/acp-11-3743-2011, 2011.

Dee, D. P., Uppala, S. M., Simmons, A. J., Berrisford, P., Poli, P., Kobayashi, S., and Bechtold, P.: The ERA‐Interim reanalysis: Configuration and performance of the data assimilation system, Q. J. Roy. Meteorol. Soc., 137, 553-597, 2011.

Draxler, R., and Rolph, G.: HYSPLIT (HYbrid Single-Particle Lagrangian Integrated Trajectory) Model access via NOAA ARL READY, NOAA Air Resources Laboratory, Silver Spring, MD, 2003.

Ehn, M., Vuollekoski, H., Petäjä, T., Kerminen, V.-M., Vana, M., Aalto, P., de Leeuw, G., Ceburnis, D., Dupuy, R., O'Dowd, C. D., and Kulmala, M.: Growth rates during coastal and marine new particle formation in western Ireland, J. Geophys. Res., 115, n/a-n/a, 10.1029/2010JD014292, 2010.

Flyger, H., and Heidam, N. Z.: Ground level measurements of the summer tropospheric aerosol in Northern Greenland, J. Aerosol Sci., 9, 157-168, 1978.

Galí, M., Devred, E., Levasseur, M., Royer, S.-J., and Babin, M.: A remote sensing algorithm for planktonic dimethylsulfoniopropionate (DMSP) and an analysis of global patterns, Remote Sens. Environ., 171, 171-184, http://dx.doi.org/10.1016/j.rse.2015.10.012, 2015.

Galí, M., and Simó, R.: A meta‐analysis of oceanic DMS and DMSP cycling processes: Disentangling the summer paradox, Global Biochem. Cycles, 29, 496-515, 2015.

1114 Gao, Q., Leck, C., Rauschenberg, C., and Matrai, P. A.: On the chemical dynamics of
1115 extracellular polysaccharides in the high Arctic surface microlayer, Ocean Sci.
1116 Discuss., 9, 215–259, 2012.
1117 Heintzenberg, J., Bischof, W., Odh, S.-Å., and Moberg, B.: An investigation of possible sites
1118 for a background monitoring station in the European Arctic., International
1119 Meteorological Institute in Stockholm, Department of Meteorology, Stockholm
1120 University, Stockholm, Report Nr. AP-22, 74 pp, 1983.
1121 Heintzenberg, J., and Larssen, S.: $SO_2$ and $SO_4$ in the Arctic: Interpretation of observations at
1122 three Norwegian Arctic-subArctic stations, Tellus, 35B, 255-265, 1983.
1123 Heintzenberg, J.: Arctic haze: air pollution in polar regions, AMBIO, 18, 50-55, 1989.
1124 Heintzenberg, J., and Leck, C.: Seasonal variation of the atmospheric aerosol near the top of
1125 the marine boundary layer over Spitsbergen related to the Arctic sulphur cycle, Tellus,
1126 46B, 52-67, 1994.
1127 Heintzenberg, J., Leck, C., Birmili, W., Wehner, B., Tjernström, M., and Wiedensohler, A.:
1128 Aerosol number-size distributions during clear and fog periods in the summer high
1129 Arctic: 1991, 1996, and 2001, Tellus, 58B, 41-50, 2006.
1130 Heintzenberg, J., Wehner, B., and Birmili, W.: "How to find bananas in the atmospheric
1131 aerosol" New approach for analyzing atmospheric nucleation and growth events,
1132 Tellus B, 59, 273-282, 2007.
1133 Heintzenberg, J.: The aerosol-cloud-climate conundrum, IJGW, 4, 219-241, 2012.
1134 Heintzenberg, J., Leck, C., and Tunved, P.: Potential source regions and processes of aerosol
1135 in the summer Arctic, Atmos. Chem. Phys., 15, 6487-6502, 10.5194/acp-15-6487-
1136 2015, 2015.
1137 Held, A., Brooks, I. M., Leck, C., and Tjernström, M.: On the potential contribution of open
1138 lead particle emissions to the central Arctic aerosol concentration, Atmos. Chem.
1139 Phys., 11, 3093-3105, 10.5194/acp-11-3093-2011, 2011a.
1140 Held, A., Orsini, D. A., Vaattovaara, P., Tjernström, M., and Leck, C.: Near-surface profiles
1141 of aerosol number concentration and temperature over the Arctic Ocean, Atmos.
1142 Meas. Tech., 4, 1603–1616, 2011b.
1143 Hubanks, P., Platnick, S., King, M., and Ridgway, B.: MODIS Atmosphere L3 Gridded
1144 Product Algorithm Theoretical Basis, Document (ATBD) and Users Guide, 2015.
1145 Huschke, R. E.: Arctic cloud statistics from "air calibrated" surface weather observations,
1146 Rand Corporation Memo. RM 6173-PR, 79 pp, 1969.

IOCCG: Ocean Colour Remote Sensing in Polar Seas, Report 16, Eds. Babin, M., Arrigo, K., Bélanger, S. and Forget, M.-H., 129 pp, 2015.

Jaenicke, R., and Schütz, L.: Arctic aerosols in surface air, Idöjaras, 86, 235-241, 1982.

Junge, C. E.: Air chemistry and Radioactivity, Academic Press, New York and London, 382 pp., 1963.

Junninen, H., Hulkkonen, M., Riipinen, I., Nieminen, T., Hirsikko, A., Suni, T., Boy, M., Lee, S.-H., Vana, M., Tammet, H., Kerminen, V.-M., and Kulmala, M.: Observations on nocturnal growth of atmospheric clusters, Tellus B, 60, 365-371, 2008.

Karl, M., Gross, A., Leck, C., and Pirjola, L.: Intercomparison of dimethylsulfide oxidation mechanisms for the marine boundary layer: Gaseous and particulate sulfur constituents, J. Geophys. Res., 112, D15304, 10.1029/2006JD007914, 2007.

Karl, M., Leck, C., Gross, A., and Pirjola, L.: A Study of New Particle Formation in the Marine Boundary Layer Over the Central Arctic Ocean using a Flexible Multicomponent Aerosol Dynamic Model, Tellus, 64B, doi:http://dx.doi.org/10.3402/tellusb.v3464i3400.17158, 2012.

Karl, M., Leck, C., Coz, E., and Heintzenberg, J.: Marine nanogels as a source of atmospheric nanoparticles in the high Arctic, Geophys. Res. Lett., 40, 3738–3743, DOI: 10.1002/grl.50661, 2013.

Keene, W. C., Pszenny, A. A. P., Galloway, J. N., and Hawley, M. E.: Sea-salt corrections and interpretation of constituent ratios in marine precipitation, J. Geophys. Res., 91, 6647-6658, 1986.

Keller, M. D., Bellows, W. K., and Guillard, R. R. L.: A survey of dimethylsulfide production in 12 classes of marine phytoplankton, in: Biogenic sulfur in the environment, edited by: E.S. Saltzman, and Cooper, W. J., American Chemical Society, Washington, D, 167–182, 1989.

King, M. D., Platnick, S., Menzel, W. P., Ackerman, S. A., and Hubanks, P. A.: Spatial and temporal distribution of clouds observed by MODIS onboard the Terra and Aqua satellites, IEEE Trans. Geosci. Remote Sens., 51, 3826–3852, 2013.

Knutson, E. O., and Whitby, K. T.: Accurate Measurement of Aerosol Electrical Mobility Moments, J. Aerosol Sci., 6, 453-460, 1975a.

Knutson, E. O., and Whitby, K. T.: Aerosol classification by electric mobility: apparatus, theory, and applications, J. Aerosol Sci., 6, 443-451, 1975b.

1179 Kulmala, M., Dal Maso, M., Mäkelä, J. M., Pirjola, L., Väkevä, M., Aalto, P. P.,
1180 Miikkulainen, P., Hämeri, K., and O'Dowd, C. D.: On the formation, growth and
1181 composition of nucleation mode particles, Tellus, 53B, 479-490, 2001.
1182 Kulmala, M., Vehkamäkia, H., Petäjä, T., Dal Maso, M., Lauri, A., Kerminen, V.-M., Birmili,
1183 W., and McMurry, P. H.: Formation and growth rates of ultrafine atmospheric
1184 particles: a review of observations, J. Aerosol Sci., 35, 143-176, 2004.
1185 Kulmala, M., Petäjä, T., Nieminen, T., Sipilä, M., Manninen, H. E., Lehtipalo, K., Dal Maso,
1186 M., Aalto, P. P., Junninen, H., Paasonen, P., Riipinen, I., Lehtinen, K. E. J.,
1187 Laaksonen, A., and Kerminen, V.-M.: Measurement of the nucleation of atmospheric
1188 aerosol particles, Nat. Protocols, 7, 1651-1667,
1189 http://www.nature.com/nprot/journal/v7/n9/abs/nprot.2012.091.html - supplementary-
1190 information, 2012.
1191 Lana, A., Simó, R., Vallina, S. M., and Dachs, J.: Re-examination of global emerging patterns
1192 of ocean DMS concentration, Biogeochem., 110, 173-182, 2012.
1193 Lannefors, H., Heintzenberg, J., and Hansson, H.-C.: A comprehensive study of physical and
1194 chemical parameters of the Arctic summer aerosol; results from the Swedish
1195 expedition Ymer-80, Tellus, 35B, 40-54, 1983.
1196 Leck, C., and Persson, C.: The central Arctic Ocean as a source of dimethyl sulfide: Seasonal
1197 variability in relation to biological activity, Tellus, 48B, 156-177, 1996a.
1198 Leck, C., and Persson, C.: Seasonal and short-term variability in dimethyl sulfide, sulfur
1199 dioxide and biogenic sulfur and sea salt aerosol particles in the arctic marine boundary
1200 layer, during summer and autumn, Tellus, 48B, 272-299, 1996b.
1201 Leck, C., and Bigg, E. K.: Aerosol production over remote marine areas - A new route,
1202 Geophys. Res. Lett., 23, 3577-3581, 1999.
1203 Leck, C., and Bigg, E. K.: New particle formation of marine biological origin, Aerosol Sci.
1204 Technol., 44, 570-577, 2010.
1205 Leck, C., Gao, Q., Mashayekhy Rad, F., and Nilsson, U.: Size-resolved atmospheric
1206 particulate polysaccharides in the high summer Arctic, Atmos. Chem. Phys., 13,
1207 12573-12588, 10.5194/acp-13-12573-2013, 2013.
1208 Lindsay, R., Wensnahan, M., Schweiger, A., and Zhang, J.: Evaluation of seven different
1209 atmospheric reanalysis products in the Arctic, J. Clim., 27, 2588-2606, 2014.
1210 Liss, P. S., and Merlivat, L.: Air-sea gas exchange rates: Introduction and synthesis, in: The
1211 Role of Air-Sea Exchange in Geochemical Cycling, edited by: Buat-Menard, P.,
1212 Reidel, Norwell, MS, 113-127, 1986.

1213 Maritorena, S., Siegel, D. A., and Peterson, A. R.: Optimization of a semianalytical ocean
1214 color model for global-scale applications, Appl. Opt., 41.15, 2705-2714, 2002.
1215 Matrai, P. A., and Vernet, M.: Dynamics of the vernal bloom in the marginal ice zone of the
1216 Barents Sea: Dimethyl sulfide and dimethylsulfoniopropionate budgets, Journal of
1217 Geophysical Research: Oceans, 102, 22965-22979, 10.1029/96JC03870, 1997.
1218 Nguyen, Q. T., Glasius, M., Sørensen, L. L., Jensen, B., Skov, H., Birmili, W., Wiedensohler,
1219 A., Kristensson, A., Nøjgaard, J. K., and Massling, A.: Seasonal variation of
1220 atmospheric particle number concentrations, new particle formation and atmospheric
1221 oxidation capacity at the high Arctic site Villum Research Station, Station Nord,
1222 Atmos. Chem. Phys., 16, 11319–11336, 10.5194/acp-2016-205, 2016.
1223 Norman, A. L., Barrie, L. A., Toom-Sauntry, D., Sirois, A., Krouse, H. R., Li, S. M., and
1224 Sharma, S.: Sources of aerosol sulphate at Alert: Apportionment using stable isotopes,
1225 J. Geophys. Res., 104, 11619-11631, 1999.
1226 O'Dowd, C., Monahan, C., and Dall'Osto, M.: On the occurrence of open ocean particle
1227 production and growth events, Geophys. Res. Lett., 37, L19805,
1228 doi:19810.11029/12010GL044679, 2010.
1229 Ogren, J. A., and Heintzenberg, J.: Parametric aerosol sampling at low concentration levels,
1230 Department of Meteorology, Stockholm UniversityAA-1, 1990.
1231 Orellana, M. V., Matrai, P. A., Janer, M., and Rauschenberg, C. D.:
1232 Dimethylsulfoniopropionate storage in *Phaecystis* (Prymnesiophyceae) secretory
1233 vesicles J. Phycol., 47, 112-117, 10.1111/j.1529-8817.2010.00936.x, 2011a.
1234 Orellana, M. V., Matrai, P. A., Leck, C., Rauschenberg, C. D., Lee, A. M., and Coz, E.:
1235 Marine microgels as a source of cloud condensation nuclei in the high Arctic, PNAS,
1236 108, 13612–13617, 2011b.
1237 Pierce, J. R., Westervelt, D. M., Atwood, S. A., Barnes, E. A., and Leaitch, W. R.: New-
1238 particle formation, growth and climate-relevant particle production in Egbert, Canada:
1239 analysis from 1 year of size-distribution observations, Atmos. Chem. Phys., 14, 8647-
1240 8663, 10.5194/acp-14-8647-2014, 2014.
1241 Pirjola, L., Kulmala, M., Wilck, M., Bischoff, A., Stratmann, F., and Otto, E.: Formation of
1242 sulphuric acid aerosols and cloud condensation nuclei: An expression for significant
1243 nucleation and model comparison, J. Aerosol Sci., 30, 1079-1094, 1999.
1244 Polissar, A. V., Hopke, P. K., Paatero, P., Kaufman, Y. J., Hall, D. K., Bodhaine, B. A.,
1245 Dutton, E. G., and Harris, J. M.: The aerosol at Barrow, Alaska: long-term trends and
1246 source locations, Atmos. Environ., 33, 2441-2458, 1999.

1247 Rahn, K. A., and Shaw, G. E.: Particulate air pollution in the Arctic: Large-scale occurence
1248 and meteorological controls, in: Atmospheric Aerosols and Nuclei, edited by: Roddy,
1249 F., and O'Connor, T. C., Dept. of Physics, University College, Galway, Ireland 21-27
1250 Sept., 223-227, 1977.
1251 Ristovski, Z. D., Suni, T., Kulmala, M., Boy, M., Meyer, N. K., Duplissy, J., Turnipseed, A.,
1252 Morawska, L., and Baltensperger, U.: The role of sulphates and organic vapours in
1253 growth of newly formed particles in a eucalypt forest, Atmos. Chem. Phys., 10, 2919-
1254 2926, 10.5194/acp-10-2919-2010, 2010.
1255 Rudels, B., Björk, G., Nilsson, J., Winsor, P., Lake, I., and Nohr, C.: The interaction between
1256 waters from the Arctic Ocean and the Nordic Seas north of Fram Strait and along the
1257 East Greenland Current: results from the Arctic Ocean-02 Oden expedition, Journal of
1258 Marine Systems, 55, 1-30, 2005.
1259 Schmidtko, S., Johnson, G. C., and Lyman, J. M.: MIMOC: A global monthly isopycnal
1260 upper-ocean climatology with mixed layers, Journal of Geophysical Research:
1261 Oceans, 118, 1658-1672, 10.1002/jgrc.20122, 2013.
1262 Schoemann, V., Becquevort, S., Stefels, J., Rousseau, V., and Lancelot, C.: Phaeocystis
1263 blooms in the global ocean and their controlling mechanisms: a review, Journal of Sea
1264 Research, 53, 43-66, http://dx.doi.org/10.1016/j.seares.2004.01.008, 2005.
1265 Sharma, S., Chan, E., Ishizawa, M., Toom-Sauntry, D., Gong, S. L., Li, S. M., Tarasick, D.
1266 W., Leaitch, W. R., Norman, A., Quinn, P. K., Bates, T. S., Levasseur, M., Barrie, L.
1267 A., and Maenhaut, W.: Influence of transport and ocean ice extent on biogenic aerosol
1268 sulfur in the Arctic atmosphere, J. Geophys. Res., 117, D12209,
1269 10.1029/2011JD017074, 2012.
1270 Simó, R.: Production of atmospheric sulfur by oceanic plankton: biogeochemical, ecological
1271 and evolutionary links, Trends in Ecology & Evolution, 16, 287-294, 2001.
1272 Stohl, A.: Computations, accuracy and applications of trajectories - A review and
1273 bibliography, Atmos. Environ., 32, 947-966, 1998.
1274 Ström, J., Engvall, A.-C., Delbart, F., Krejci, R., and Treffeisen, R.: On small particles in the
1275 Arctic summer boundary layer: observations at two different heights near Ny-Ålesund,
1276 Svalbard, Tellus B - Chemical and Physical Meteorology, 61, 473-482, 2009.
1277 Suni, T., Kulmala, M., Hirsikko, A., Bergman, T., Laakso, L., Aalto, P. P., Leuning, R.,
1278 Cleugh, H., Zegelin, S., Hughes, D., van Gorsel, E., Kitchen, M., Vana, M., Hõrrak,
1279 U., Mirme, S., Mirme, A., Sevanto, S., Twining, J., and Tadros, C.: Formation and

characteristics of ions and charged aerosol particles in a native Australian Eucalypt forest, Atmos. Chem. Phys., 8, 129-139, 10.5194/acp-8-129-2008, 2008.

Tunved, P., Ström, J., and Krejci, R.: Arctic aerosol life cycle: linking aerosol size distributions observed between 2000 and 2010 with air mass transport and precipitation at Zeppelin station, Ny-Ålesund, Svalbard, Atmos. Chem. Phys., 13, 3643–3660, 10.5194/acpd-12-29967-2012, 2013.

Venzac, H., Sellegri, K., Villani, P., Picard, D., and Laj, P.: Seasonal variation of aerosol size distributions in the free troposphere and residual layer at the Puy de Dôme station, France, Atmos. Chem. Phys., 9, 1465-1478, 10.5194/acp-9-1465-2009, 2009.

Warren, S. G., and Hahn, C. J.: Cloud climatology, in: Encyclopedia of Atmospheric Sciences, edited by: Holton, J. R., Pyle, J., and Curry, J. A., Academic Press, London, UK, 476-483, 2002.

Wiedensohler, A., Covert, D., Swietlicki, E., Aalto, P., Heintzenberg, J., and Leck, C.: Occurrence of an ultrafine particle mode less than 20 nm in diameter in the marine boundary layer of the Arctic summer and autumn, Tellus, 48B, 213-222, 1996.

Willis, M. D., Burkart, J., Thomas, J. L., Köllner, F., Schneider, J., Bozem, H., Hoor, P. M., Aliabadi, A. A., Schulz, H., Herber, A. B., Leaitch, W. R., and Abbatt, J. P. D.: Growth of nucleation mode particles in the summertime Arctic: a case study, Atmos. Chem. Phys. Discuss., 2016, 1-31, 10.5194/acp-2016-256, 2016.

Yli-Juuti, T., Riipinen, I., Pasi, A., Nieminen, T., Maenhaut, W., Janssens, A., Claeys, M., Salma, I., Ocskay, R., Hoffer, A., Imre, K., and Kulmala, M.: Characteristics of new particle formation events and cluster ions at K-puszta, Hungary, Boreal Environment Research\, 14\, 2009.

Young, L. H., Lee, S. H., Kanawade, V. P., Hsiao, T. C., Lee, Y. L., Hwang, B. F., Liou, Y. J., Hsu, H. T., and Tsai, P. J.: New particle growth and shrinkage observed in subtropical environments, Atmos. Chem. Phys., 13, 547-564, 10.5194/acp-13-547-2013, 2013.

Zhang, M., Chen, L., Xu, G., Lin, Q., and Liang, M.: Linking Phytoplankton Activity in Polynyas and Sulfur Aerosols over Zhongshan Station, East Antarctica, J. Atmos. Sci., 72, 4629-4642, 2015.

| Parameter | TR (h) | Explanation |
|---|---|---|
| C25 | 1 min | 25% percentile of cloud base from AWI ceilometer (m) |
| CF12, 24, 36, 48, 5D | 24 | Average MODIS cloud fraction during the last 12h, 24h, 36, 48h, and days 3-5 before trajectory arrival |
| D50 | 1 | Number-median diameter of particles < 50 nm diameter |
| CS | 1 | Condensation sink ($s^{-1}$) |
| DZ | 1 | Vertical trajectory displacement (m $h^{-1}$) during the last hour before arrival |
| MSA | ≥1 day | Methane sulfonate ($nmolm^{-3}$) |
| N10 | 1 | Number concentration of particles up to 10 nm (>2010, $cm^{-3}$) |
| N20 | 1 | Number concentration between 10 and 20 nm ($cm^{-3}$) |
| N25 | 1 | Number concentration of particles up to 25 nm ($cm^{-3}$) |
| N40 | 1 | Number concentration between 20 and 40 nm ($cm^{-3}$) |
| N60 | 1 | Number concentration between 40 and 60 nm ($cm^{-3}$) |
| N100 | 1 | Number concentration between 60 and 100 nm ($cm^{-3}$) |
| N300 | 1 | Number concentration between 100 and 300 nm ($cm^{-3}$) |
| Na | ≥1 day | Sodium concentrations ($nmolm^{-3}$) |
| NCO | 1 | Number concentration of particles > 300 nm ($cm^{-3}$) |
| $nssSO_4^{2-}$ | ≥1 day | Non-sea salt sulfate concentrations ($nmolm^{-3}$) |
| NTO | 1 | Number concentration of particles ≥ 10 nm, $cm^{-3}$) |
| OC12, 24, 36, 48, 5D | 120 | Average MODIS DMSPt (nmol) during the last 12h, 24h, 36, 48h, and days 3-5 before trajectory arrival |
| OW12, 24, 36, 48, 5D | 24 | Average open water (%) during the last 12h, 24h, 36, 48h, and days 3-5 before trajectory arrival |
| PRE | 1 | Trajectory precipitation (mm) at arrival |
| RH | 1 | Trajectory relative humidity (%) at arrival |
| SFL | 1 | Solar flux at trajectory arrival ($Wm^{-2}$) |
| SP12, 24, 36, 48, 5D | 1 | Accumulated precipitation (mm) during the last 12h, 24h, 36, 48h, and days 3-5 before trajectory arrival |
| T12, 24, 36, 48, 5D | 24 | Average sea surface temperature (C) during the last 12h, 24h, 36, 48h, and days 3-5 before trajectory arrival |
| TEM | 1 | Trajectory temperature (C) at arrival |
| WDR | 1 | Trajectory wind direction (°) during the last hour before arrival |
| WSP | 1 | Trajectory wind speed (m $sec^{-1}$) during the last hour before arrival |

Table 1 Aerosol, atmospheric, and ocean parameters utilized in the present study. DMSPt = Total dimethylsulfoniopropionate in surface ocean waters. TR = temporal resolution in which the respective data were available. All parameter explanations starting with "Trajectory" refer to parameters calculated by HYSPLIT4 at each trajectory step.

| Approach | Acronym | Criteria and thresholds | Total number of events | Number of unique events | % of total number of data hours |
|---|---|---|---|---|---|
| Percentiles | PCT | N25 >93%-percentile | 4143 | 240 | 1 |
| Diameter-growth | DGR | D50-Growth >1.5 | 1199 | 235 | 3 |
| Multi-size growth | MEV | Multi-growth >1.6 | 1191 | 266 | 4 |
| Sum | | | 6533 | 741 | |

Table 2 Total and unique number of events of new particle formation identified by the three approaches to identify NPF-events, and percent of all data hours covered by unique events.

| Statistics | J11 | GR11 | J22 | GR22 |
|---|---|---|---|---|
| Minimum | 0.1 | -1.2 | 0.1 | -0.1 |
| 25% | 0.4 | 0.1 | 0.2 | 1.0 |
| 50% | 0.7 | 0.4 | 0.3 | 1.4 |
| 75% | 1.4 | 0.6 | 0.7 | 1.8 |
| Maximum | 19 | 2.2 | 22 | 4 |

Table 3 Statistics of particle formation rates of DGR-events J11, and J22, ($cm^{-3}s^{-1}$), at the nominal geometric mean diameters 11 nm, and 22 nm and corresponding diameter growth rates GR11, and GR22, ($nmh^{-1}$) in the two diameter ranges 5 – 25 nm, and 10 – 50 nm.

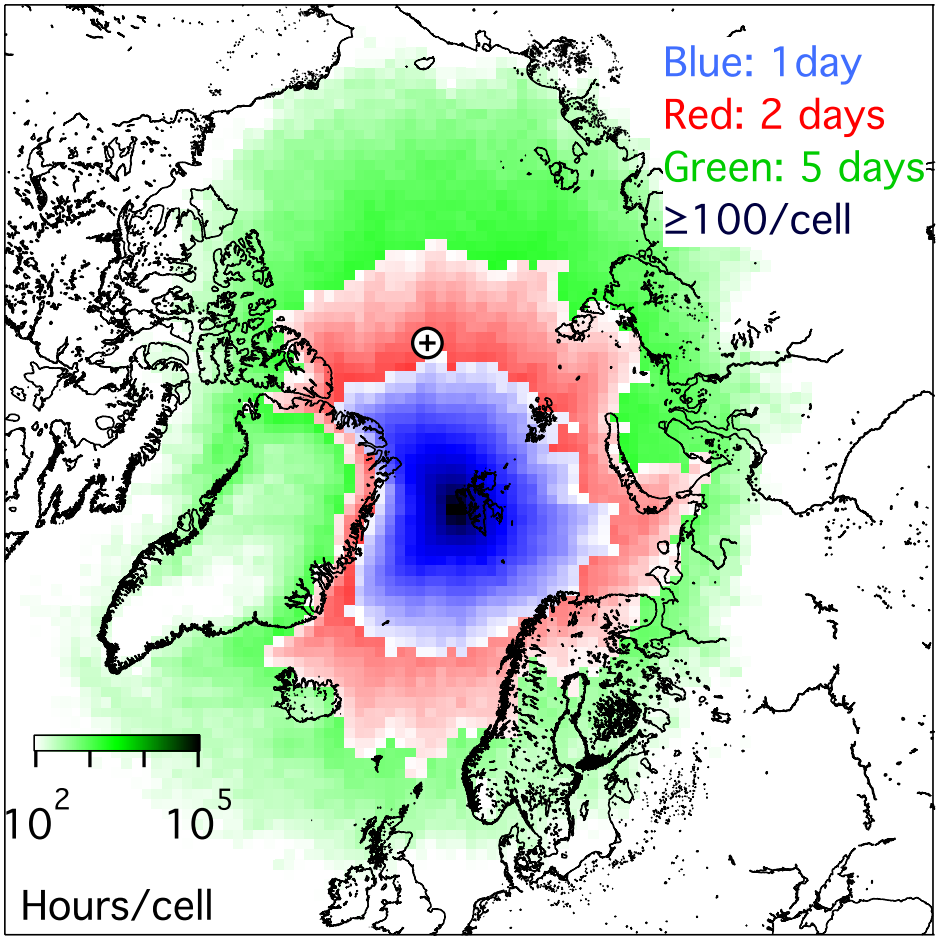


1341

1342 Fig. 1 Map of the regional distribution of 5-day (green), 2-day (red), and 1-day (blue)
1343 hourly back trajectories to Mt. Zeppelin during the months March through October
1344 of the years 2006 - 2015. Black symbol: North Pole. The colored areas are covered
1345 with at least 100 trajectory hours per geocell and the color saturation corresponds to
1346 the number of trajectory hours per grid cell on a log-scale.

1347

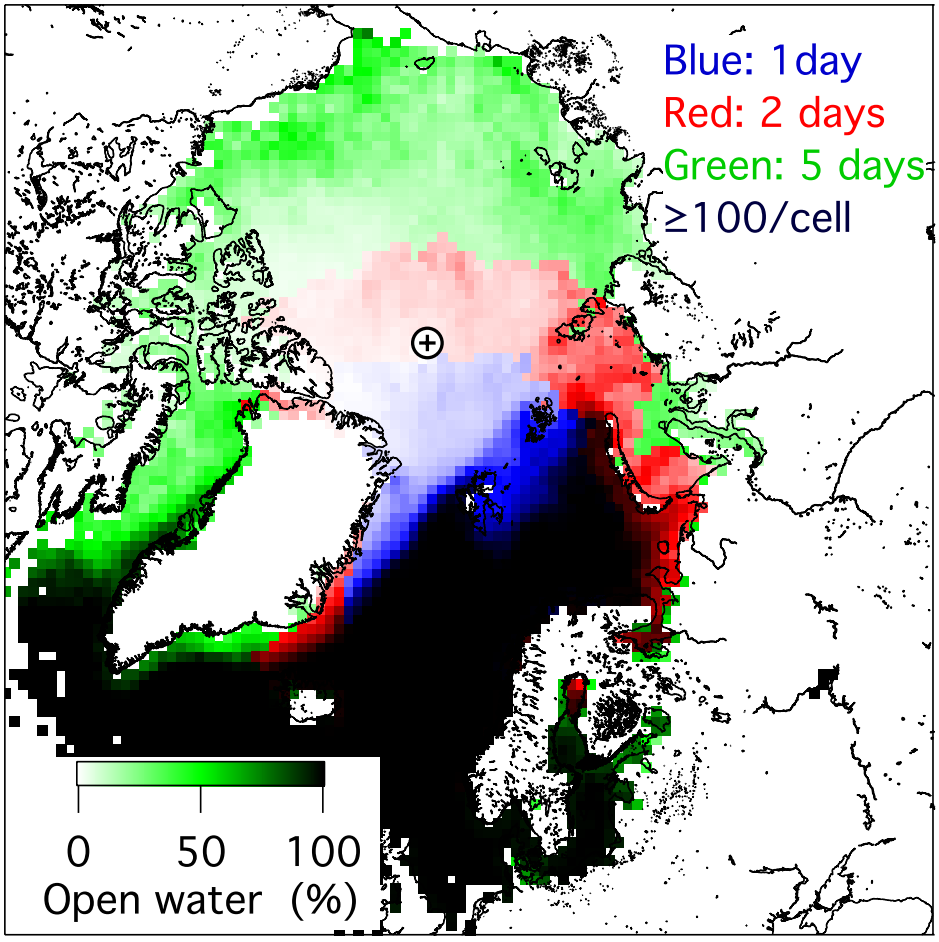


1348

1349 Fig. 2 Map of the regional distribution of open water under 87648 5-day (green), 2-day
1350 (red), and 1-day (blue) hourly back trajectories to Mt. Zeppelin during the during the
1351 months March through October of the years 2006-2015. Black symbol: North Pole.
1352 The areas are covered with at least 100 trajectory hours concurrent with data values
1353 per geocell.

1354

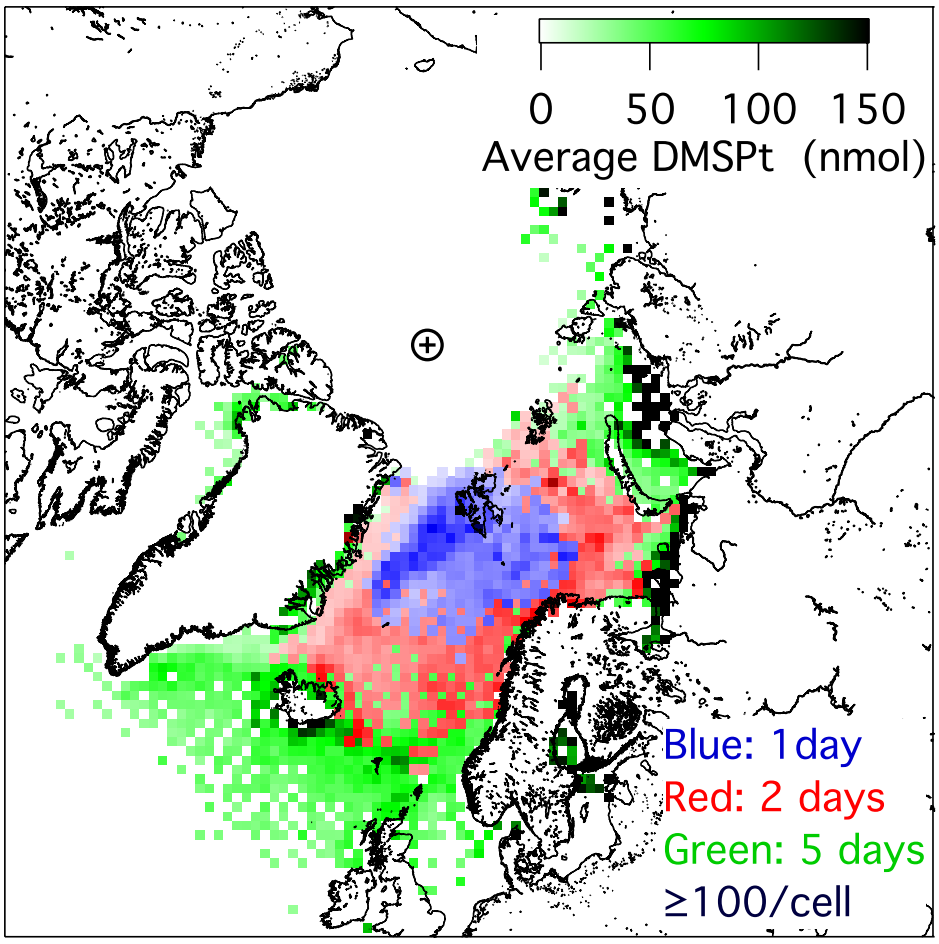


1355

1356 Fig. 3 Map of the regional distribution of DMSPt along 87648 5-day (green), 2-day (red),
1357 and 1-day (blue) hourly back trajectories to Mt. Zeppelin during the during the
1358 months March through October of the years 2006-2015. Black symbol: North Pole.
1359 The relative color scale holds for all colors. The areas are covered with at least 100
1360 trajectory hours with data values per geocell.

1361

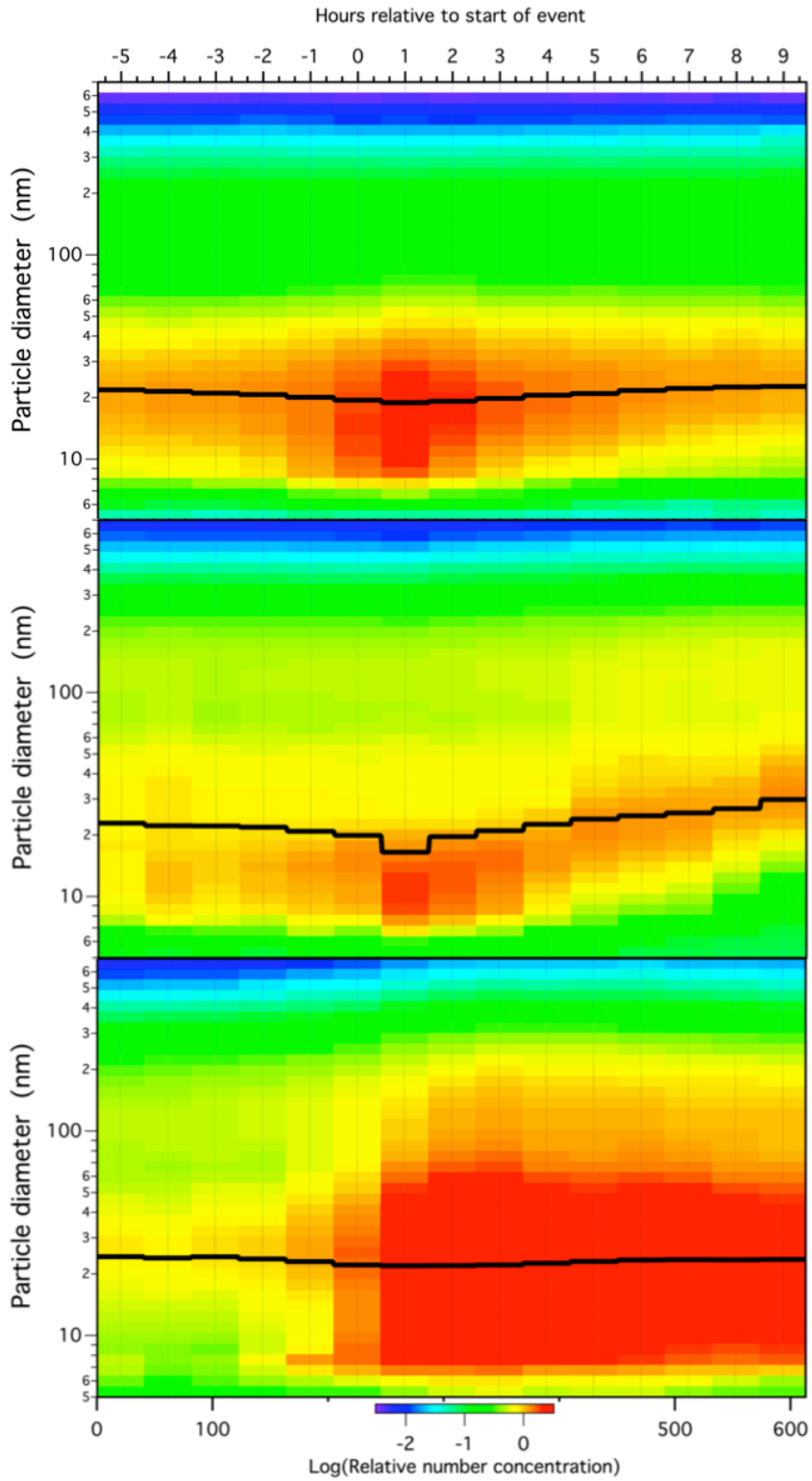


Fig.4 Average temporal development of the relative number size distribution before and during NPF-events identified by the three approaches. The black curve gives the median sub-50-nm particle diameter D50 during the events. Top: PCT-events; center: DGR-events; bottom: MEV-events.

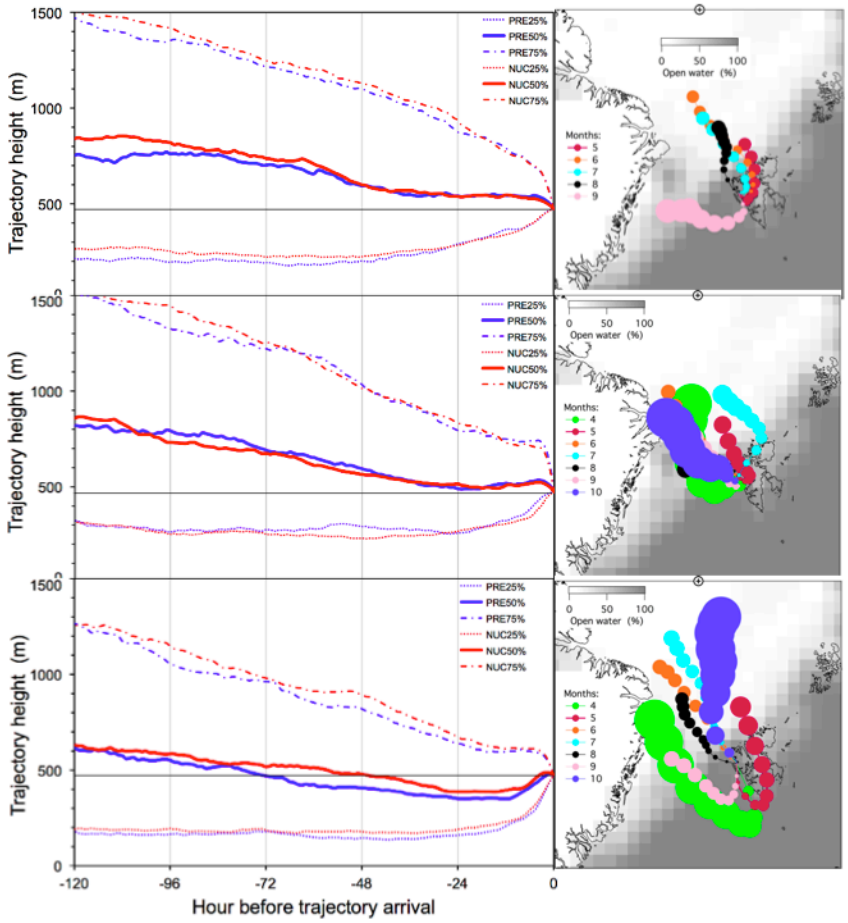


Fig. 5 Left panels: Median back trajectory height profiles (m) during the six pre-event hours (full line in blue, PRENUC) and during the nine DGR-event hours (full line in red, NUC). 25% and 75% percentiles are shown as dotted, and dash-dotted lines, respectively. Top: PCT-events; center: DGR-events; bottom: MEV-events. The thin horizontal line marks the station level.

Right panels: Average monthly trajectory positions in 12 h steps for the months April though October. Only months with at least 10 NPF-events are shown. The circles comprise 95% of all trajectories at any trajectory step. The underlying grey-scale map indicates July ice cover averaged over the years 2006 – 2015

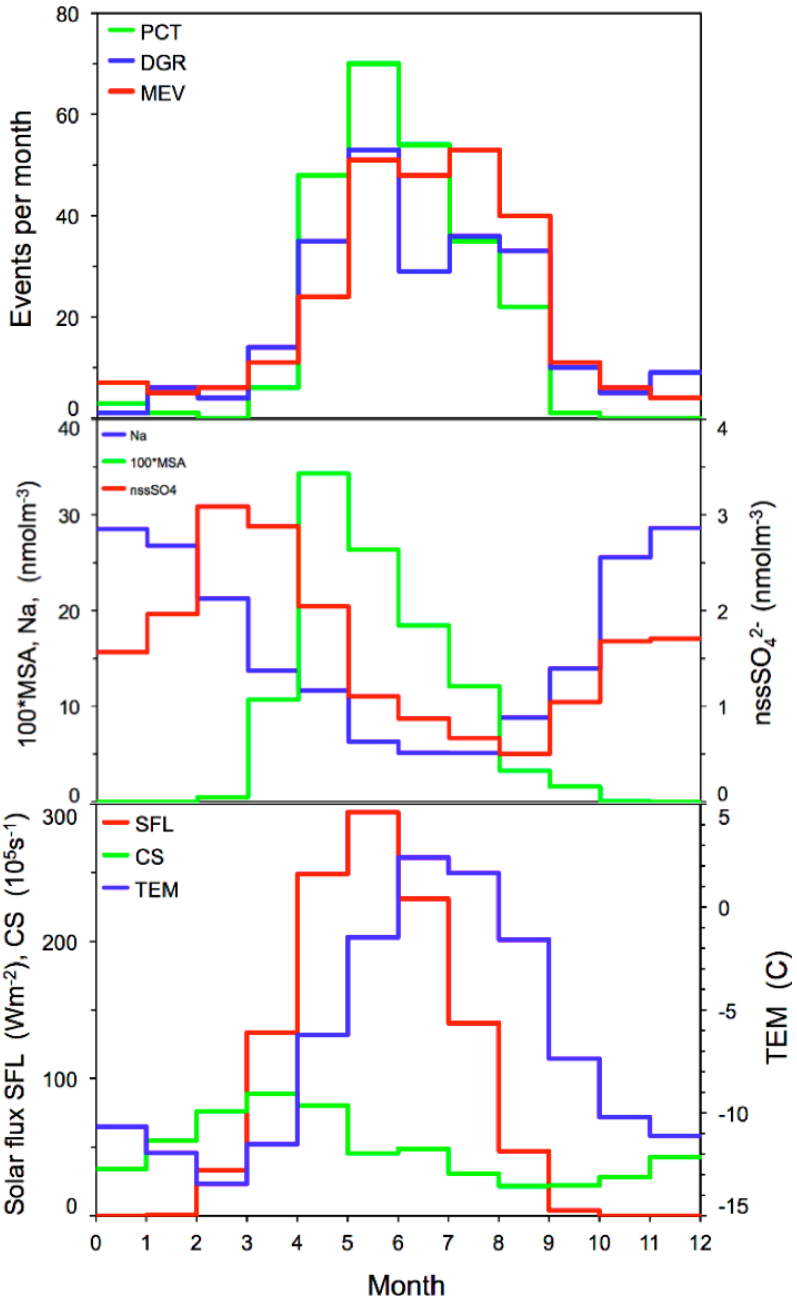


1379

1380 Fig. 6 Top: Monthly numbers of new particle formation events according to the three
1381 approaches, summed up over the whole period of ten years. PCT: Upper percentile
1382 of N25; DGR: Diameter growth; MEV: Multiple size events.
1383 Center: Average seasonal distribution of particle composition in $nmolm^{-3}$.
1384 Na = sodium, nssSO4 = $nssSO_4^{2-}$, MSA = Methane sulfonate times 100.
1385 Bottom: Monthly average solar flux (SFL, red, $Wm^{-2}$), and temperature (TEM, blue
1386 °C), and condensation sink, (CS, $10^5 s^{-1}$), at Mt. Zeppelin, Spitsbergen.

1387

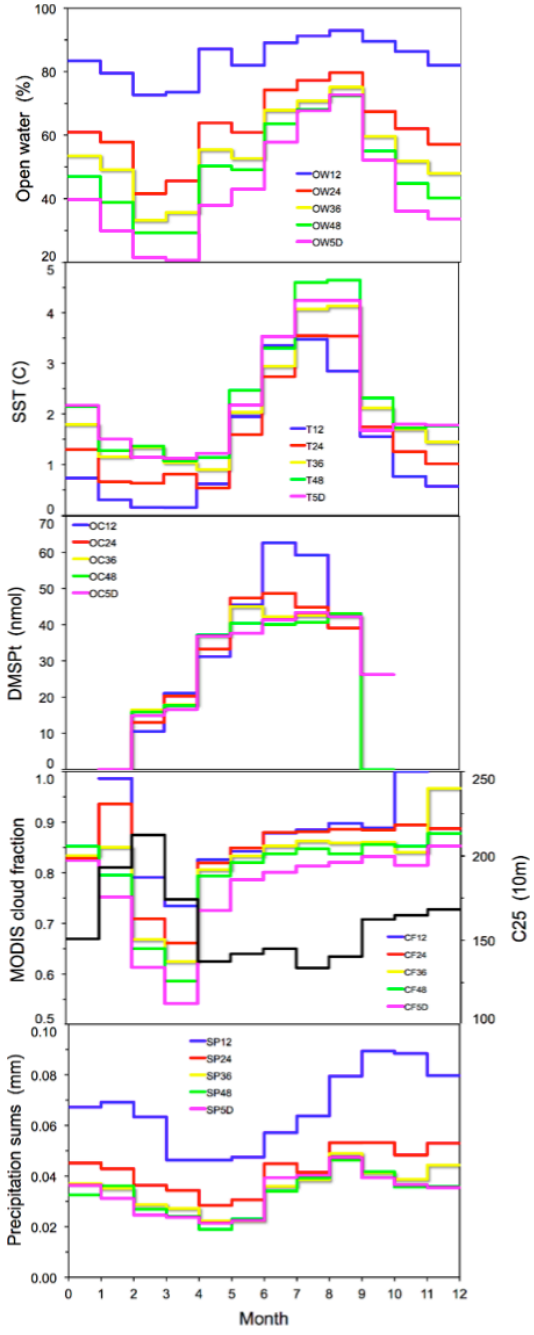


Fig. 7 Monthly averages of environmental parameters averaged along back trajectories to Mt. Zeppelin. From top to bottom: OW12-5D: Open water in % during last 12, 24, 36, and 48h, and days 3-5 before trajectory arrival at Mt. Zeppelin. T12-5D: Same for sea surface temperature in °C. OC12-5D: Same for DMSPt in nmol in surface waters. CF12-5D: Same for MODIS cloud fraction. SP12-5D: Same for precipitation sums in mm. C25 = 25%-percentile of cloud base in decameter.

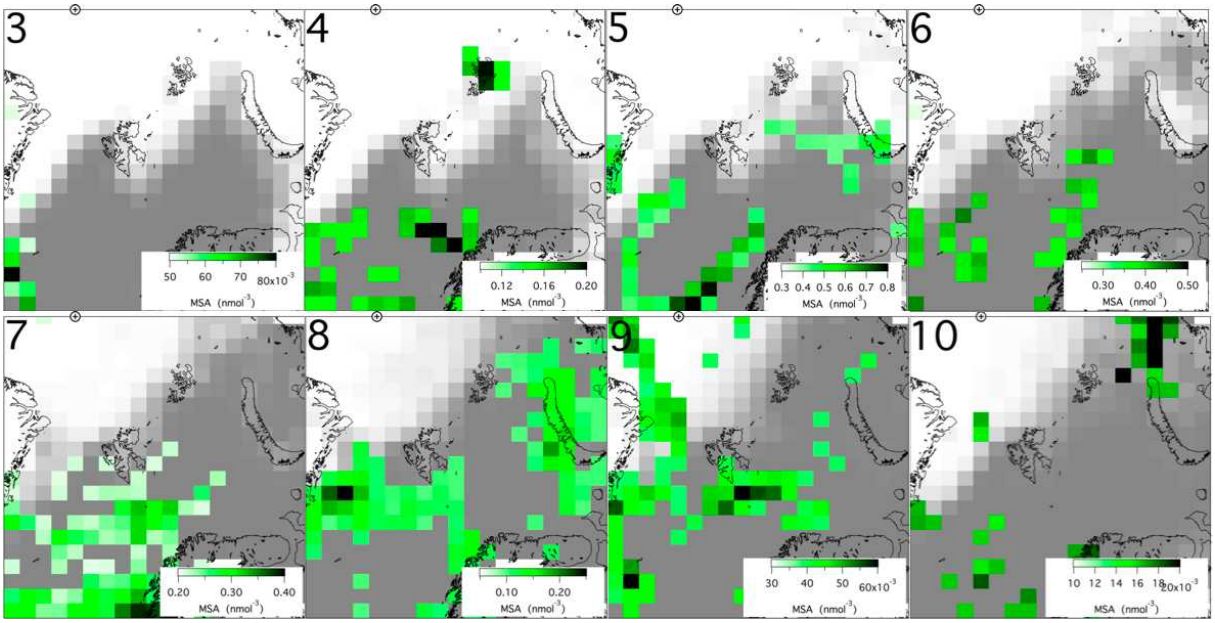


Fig. 8 Average monthly distribution of methane sulfonic acid, (MSA, $nmolm^{-3}$), during the months March – October of the years 2006 – 2015, constructed from MSA-concentrations measured on Mt. Zeppelin, which were extrapolated along 5-day back trajectories. Average open water percentages during the respective months are indicated as white (0% open water) to dark grey (100% open water) areas. The position of the North Pole is marked as cross in circle on the upper border of the maps.

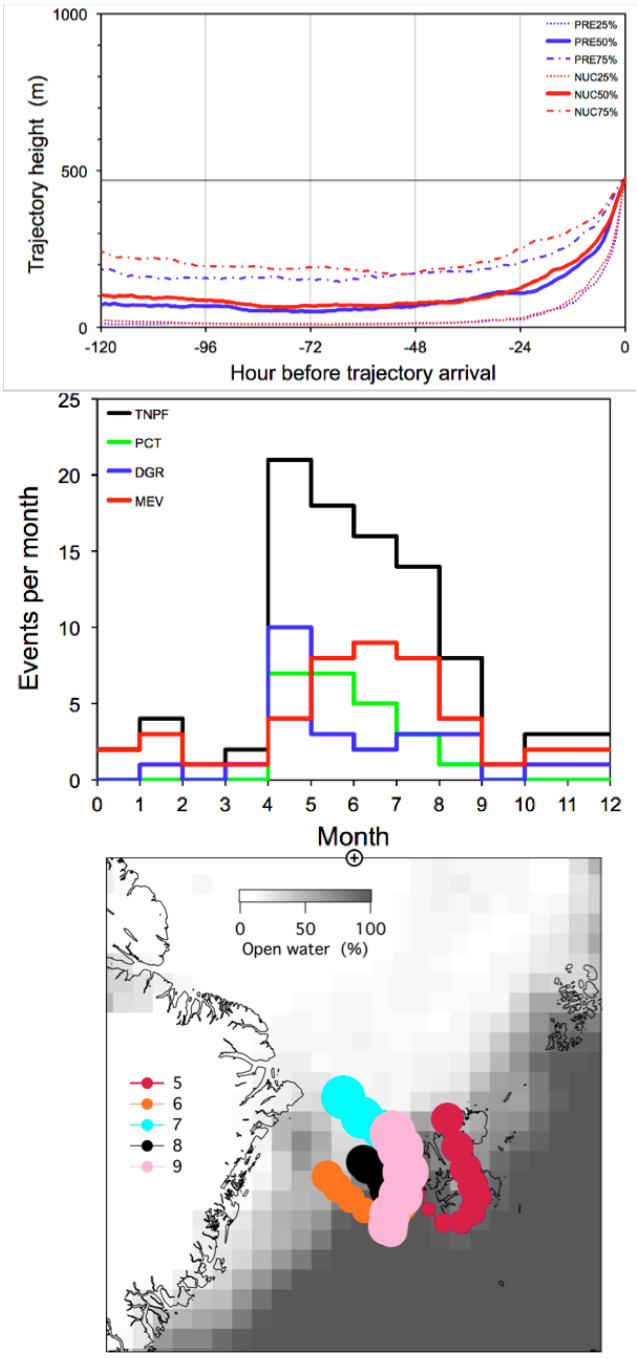


1406

1407 Fig. 9 Characteristics of the subpopulation of 93 NPF-events with back trajectories that
1408 stayed below 500 m for five days before arrival. Top: Statistics of related vertical
1409 trajectory coordinates as in Fig. 5. Center: Average monthly occurrence of PCT,
1410 DGR, and MEV-events, summed up over the whole period of ten years. Bottom:
1411 Related average monthly trajectory positions in 12 h steps for the months May
1412 through September. The circles comprise 95% of all trajectories at any trajectory

1413 step. The underlying grey-scale map indicates July ice cover averaged over 2006 –
1414 2015.
1415

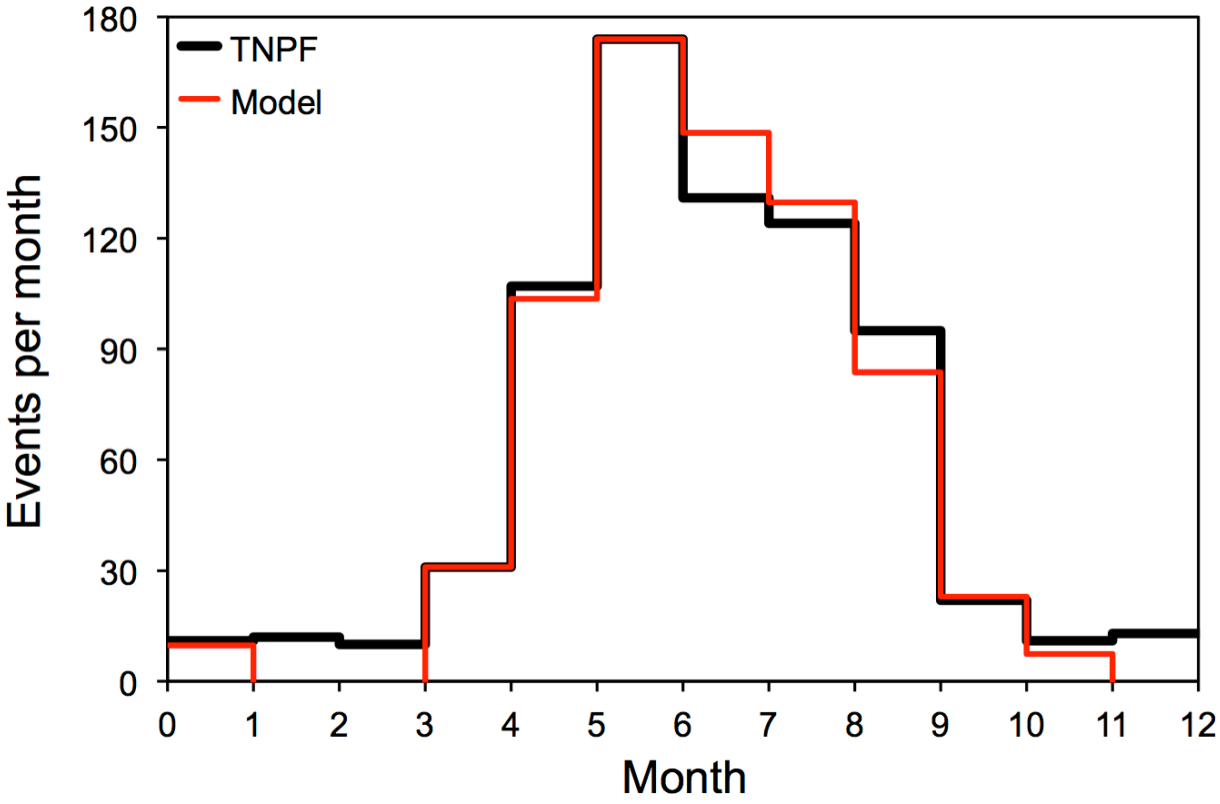


Fig. 10 Average monthly sums of NPF-events due to the three types of new particle formation, (TNPF, black), summed up over the whole period of ten years. Red: Three-parameter model to describe TNPF.

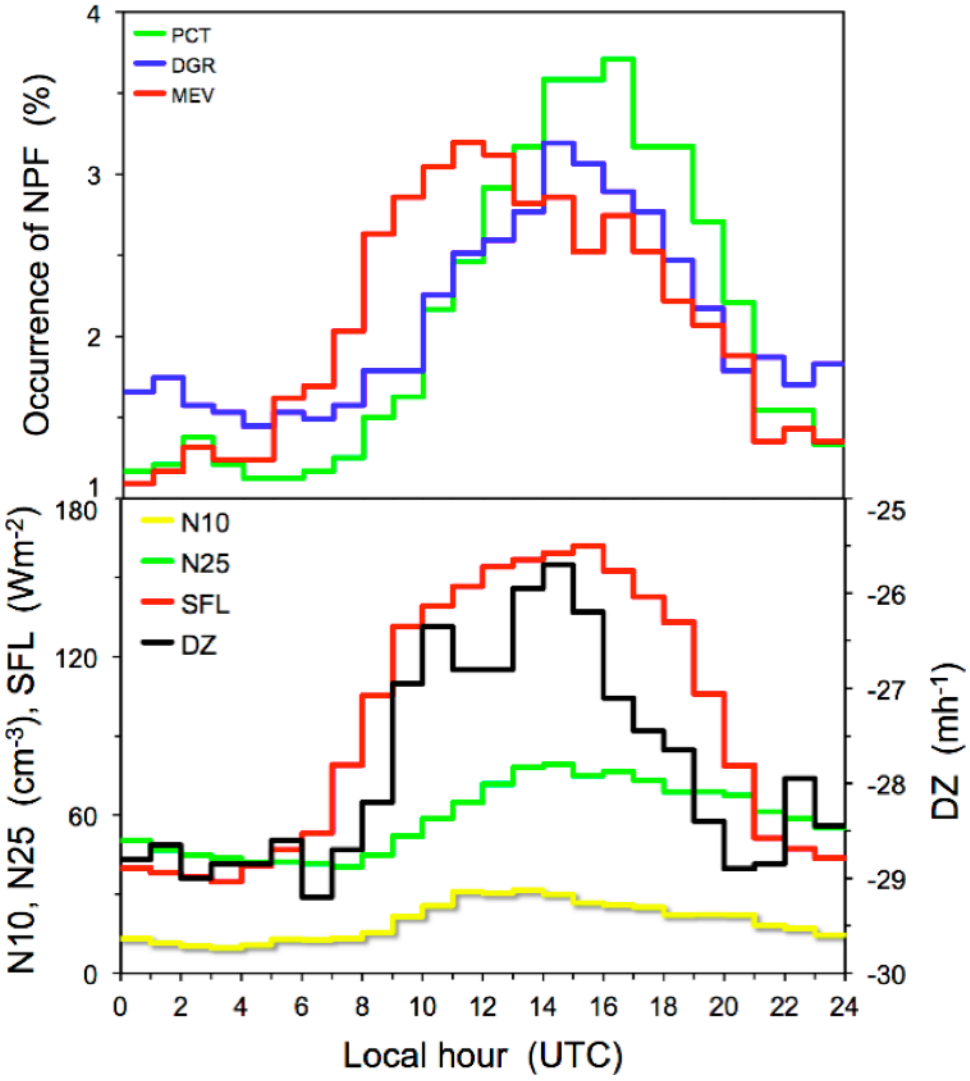


Fig. 11 Top: Relative average diurnal occurrence of the three types NPF-events. PCT: Upper percentile of N25; DGR: Diameter growth; MEV: Multiple size events. Bottom: Average diurnal variation of the HYSPLIT-modeled solar flux (SFL, $Wm^{-2}$), the integral particle concentrations N10, and N25 in $cm^{-3}$, and of the vertical displacement parameter (DZ, $mh^{-1}$). N10 is based on data of the years 2011 – 2015 whereas the other parameters are based on data of the years 2006 – 2015.